



Evaluation of NU-WRF Performance on Air Quality Simulation under Various Model Resolutions – An Investigation within Framework of MICS-Asia Phase III

Zhining Tao^{1,2}, Mian Chin², Meng Gao³, Tom Kucsera^{1,2}, Dongchul Kim^{1,2}, Huisheng Bian^{2,4}, Jun-ichi Kurokawa⁵, Yuesi Wang⁶, Gregory R. Carmichael⁷, Zifa Wang^{6,8,9}, and Hajime Akimoto¹⁰

1. Universities Space Research Association, Columbia, MD, USA
2. NASA Goddard Space Flight Center, Greenbelt, MD, USA
3. John A. Paulson School of Engineering and Applied Sciences, Harvard University, Cambridge, MA, USA
4. University of Maryland at Baltimore County, Baltimore, MD, USA
5. Japan Environmental Sanitation Center, Asia Center for Air Pollution Research, Niigata, 950-2144, Japan
6. State Key Laboratory of Atmospheric Boundary Layer Physics and Atmospheric Chemistry, Institute of Atmospheric Physics, Chinese Academy of Sciences, Beijing, 100029, China
7. Center for Global and Regional Environmental Research, University of Iowa, Iowa City, IA, USA
8. College of Earth Sciences, University of Chinese Academy of Sciences, Beijing, 100049, China
9. Center for Excellence in Urban Atmospheric Environment, Institute of Urban Environment, Chinese Academy of Sciences, Xiamen, 361021, China
10. National Institute for Environmental Studies, Onogawa, Tsukuba, 305-8506, Japan



1 **Abstract**

2

3

4 Horizontal grid resolution has a profound effect on model performances on meteorology
5 and air quality simulations. In contribution to MICS-Asia Phase III, one of whose goals was to
6 identify and reduce model uncertainty in air quality prediction, this study examined the impact of
7 grid resolution on meteorology and air quality over East Asia, focusing on the North China Plain
8 (NCP) region. NASA Unified Weather Research and Forecasting (NU-WRF) model has been
9 applied with the horizontal resolutions at 45-, 15-, and 5-km. The results revealed that, in
10 comparison with ground observations, no single resolution can yield the best model performance
11 for all variables across all stations. From a regional average perspective (i.e., across all monitoring
12 sites), air temperature modeling was not sensitive to the grid resolution but wind and precipitation
13 simulation showed the opposite. NU-WRF with the 5-km grid simulated the best wind speed, while
14 the 45-km grid yielded the most realistic precipitation as compared to the site observations. For air
15 quality simulations, finer resolution generally led to better comparisons with observations for O₃,
16 CO, NO_x, and PM_{2.5}. However, the improvement of model performance on air quality was not
17 linear with the resolution increase. The accuracy of modeled surface O₃ out of the 15-km grid was
18 greatly improved over the one from the 45-km grid. Further increase of grid resolution, however,
19 showed diminished impact on model performance on O₃ prediction. In addition, finer resolution
20 grid showed large advantage to better capture the frequency of high pollution occurrences. This
21 was important for assessment of noncompliance of ambient air quality standards, which was key
22 to air quality planning and management. Balancing the findings and resource limitation, a 15-km
23 grid resolution was suggested for future MICS-Asia air quality modeling activity. This
24 investigation also found out large overestimate of ground-level O₃ and underestimate of surface
25 NO_x and CO, likely due to missing emissions of NO_x and CO.

25

26



27 1. Introduction

28 Air pollution is a threat to human health/climate and detrimental to ecosystem (Anenberg
29 et al., 2010; <https://www.who.int/airpollution/ambient/en/>). Lelieveld et al. (2015) estimated that
30 over 3 million premature mortality could be attributable to outdoor air pollution worldwide in 2010
31 based on their analysis of data and the results from a high-resolution global air quality model.
32 Since the turn of 21st century, East Asia has undergone remarkable changes in air quality as
33 observed by satellite and ground stations (Jin et al., 2016; Krotkov et al., 2016). In the past decade,
34 haze (fine particle) pollution has become a household name in China and many severe haze events
35 have been reported and their formation mechanisms and associations with global- and meso-scale
36 meteorology have been analyzed (Zhao et al., 2013; Huang et al., 2014; Gao et al., 2016; Cai et
37 al., 2017; Zou et al., 2017). Meanwhile, ground level ozone has been a major air quality concern
38 in China (Wang et al., 2017; Lu et al., 2018), Japan (Akimoto et al., 2015), and South Korea (Seo
39 et al., 2014). In combination with observations from various platforms, chemical transport model
40 (CTM) remains an important tool to understand mechanisms, to investigate spatial-temporal
41 distributions, and to design feasible control strategies of air pollution. However, CTM model
42 uncertainties persist (e.g., Carmichael et al., 2008) and the interpretation of any model results needs
43 caution and exertion of careful analysis.

44 Inter-model comparison study provides a valuable way to understand model uncertainties
45 and sheds light on model improvements. With this as one of its major goals, the Model Inter-
46 Comparison Study for Asia (MICS-Asia) was initiated in 1998. Since then MICS-Asia has gone
47 through three phases with emphasis on various aspects of air pollution. Phase I focused on long-
48 range transport and deposition of sulfur over East Asia (Carmichael et al., 2002). Phase II expanded
49 the analysis on more pollutants including nitrogen compounds, particulate matter, and ozone, in
50 addition to sulfur (Carmichael et al., 2008). Fast moving to Phase III, MICS-Asia concentrated on
51 three topics with number one aiming at identifying strengths and weaknesses of current air quality
52 models to provide insights on reducing uncertainties (Gao et al., 2018). There are totally 14 CTMs
53 – 13 regional and 1 global – participating in the coordinated model experiment, which simulated
54 air quality over Asia throughout the year 2010. Due to the constrain of computing resources among
55 participating modeling groups, a 45-km horizontal resolution has been commanded for every team
56 to run the year-long experiment.

57 This relatively coarse spatial resolution raises the question of how representative the model
58 can resolve key issues relevant to air quality and its planning/regulation, e.g., heterogeneous
59 emissions, inhomogeneous land cover and meteorology. For example, Valari and Menut (2008)
60 explored the issue using the CHIMERE model at various horizontal resolutions over Paris. They
61 found out that the ozone simulation was especially sensitive to the resolution of emissions.
62 However, the benefit of increasing emissions resolutions to improve ozone forecast skills was not
63 monotonic and at certain point the forecast accuracy decreased upon further resolution increase.
64 Using the Weather Research and Forecasting Chemistry model (WRF-Chem) with various
65 horizontal resolution (3 ~ 24 km) over the Mexico City, Tie et al. (2010) concluded that a 1 to 6
66 ratio of grid resolution to city size appeared to be a threshold to improve ozone forecasting skill
67 over mega-city areas: the forecast would be improved significantly when model resolution was
68 below this threshold value. On contrary to Valari and Menut (2008), however, Tie et al. (2010)
69 suggested that the meteorology changes associated with the grid size choice played a more
70 prominent role in contributing to the improvement of ozone forecast skills. More recently, Neal et
71 al. (2017) employed a high-resolution (12 km) air quality model with high-resolution emissions
72 within the Met Office's Unified Model (AQUUM) for air quality forecast over the Great Britain.



73 They found out that AQUM significantly improved the forecast accuracy of primary pollutants
74 (e.g., NO₂ and SO₂) but less obviously for secondary pollutants like ozone, as compared with a
75 regional composition-climate model (RCCM, 50 km horizontal resolution). But there was a
76 drawback from their conclusion in that the chemical mechanisms and photolysis rates utilized in
77 AQUM and RCCM were different, complicating the underlying reasons for changes in forecast
78 skills. Lee et al. (2018) examined the importance of aerosol-cloud-radiation interactions to
79 precipitation and the model resolution impact of key meteorological processes that affected
80 precipitation using the Advanced Research WRF model. They found that the coarse model
81 resolution would lower updraft, alter cloud properties (e.g. mass, condensation, evaporation, and
82 deposition), and reduce cloud sensitivity to ambient aerosol changes. They further concluded that
83 the uncertainty associated with resolution was much more than that related to cloud microphysics
84 parameterization. The resultant meteorological condition change would trigger air quality response
85 as well.

86 Despite the progress, the exploration of impacts of model resolution on local air quality
87 over Asia is rare. Taking advantage of the MICS-Asia platform, we examined the issue over the
88 MICS-Asia domain using the NASA Unified WRF (NU-WRF, Tao et al., 2013, 2016, 2018;
89 Peters-Lidard et al., 2015), focusing on the North China Plain (NCP) that was plagued by frequent
90 heavy air pollution episodes. The investigation would not only assist in gaining insights on how
91 model horizontal resolution affects simulated meteorology and air quality, but also contribute to
92 formulation of uncertainties resulted from model resolutions to the MICS-Asia community. The
93 latter would especially be valuable since most MICS-Asia Phase III model simulations were
94 conducted at a specific horizontal resolution (i.e., 45-km for most participants).

95

96 **2. NU-WRF model and experiment design**

97 NU-WRF is an integrated regional Earth-system modeling system developed from the
98 advanced research version of WRF-Chem (Grell et al., 2005), which represents atmospheric
99 chemistry, aerosol, cloud, precipitation, and land processes at convection-permitting spatial scales
100 (typically 1-6 km). NU-WRF couples the community WRF-Chem with NASA's Land Information
101 System (LIS), a software framework including a suite of land surface models (LSMs) that are
102 driven by satellite/ground observations and reanalysis data (Kumar et al., 2006; Peters-Lidard et
103 al., 2007). It also couples the Goddard Chemistry Aerosol Radiation and Transport (GOCART)
104 bulk aerosol scheme (Chin et al., 2002, 2007) with the Goddard radiation (Chou and Suarez, 1999)
105 and microphysics schemes (Tao et al., 2011; Shi et al., 2014) that allows for fully coupled aerosol-
106 cloud-radiation interaction simulations. In addition, NU-WRF links to the Goddard Satellite Data
107 Simulator Unit (G-SDSU), which converts simulated atmospheric profiles, e.g. clouds,
108 precipitation, and aerosols, into radiance or backscatter signals that can directly be compared with
109 satellite level-1 measurements at a relevant spatial and temporal scale (Matsui et al., 2009, 2013,
110 2014). In this study, NU-WRF has been employed to carry out the model simulations at various
111 horizontal resolutions using the same set of physical and chemical configurations.

112

113 A nested domain setup was configured to this investigation as shown Figure 1. The 45-km
114 resolution mother domain (d01) covered the MICS-Asia Phase III study region. The nested 15-km
115 (d02) and 5-km (d03) domains covered the East Asia and NCP, respectively. This analysis focused
116 on NCP and its adjacent areas with over 1.1 million square kilometers. The key NU-WRF
117 configurations included the updated Goddard cumulus ensemble microphysics scheme (Tao et al.,
118 2011), new Goddard long/shortwave radiation scheme (Chou and Suarez, 1999), Monin-Obukhov
surface layer scheme, unified Noah land surface model (Ek et al., 2003) with LIS initialization



119 (Peters-Lidard et al., 2015), Yonsei University planetary boundary layer scheme (YSU, Hong et
120 al., 2006), new Grell cumulus scheme off the ensemble cumulus scheme (Grell and Devenyi, 2002)
121 that allowed subsidence spreading (Lin et al., 2010), 2nd generation regional acid deposition model
122 (RADM2, Stockwell et al., 1990; Gross and Stockwell, 2003) for trace gases and GOCART for
123 aerosols. In this investigation, the option of fully coupled GOCART-Goddard microphysics and
124 radiation schemes (Shi et al., 2014) has been implemented to account for the aerosol-cloud-
125 radiation interactions.

126 Anthropogenic emissions were from the mosaic Asian anthropogenic emissions inventory
127 (MIX, Li et al., 2017) that was developed for the MICS-Asia Phase III. The MIX inventory was
128 projected to the study domain under the 45-, 15-, and 5-km horizontal resolutions. Fire emissions
129 were from the Global Fire Emissions Database version 3 (GFEDv3, van der Werf et al., 2010; Mu
130 et al., 2011) and also projected to the targeted region. Biogenic emissions were computed online
131 using the Model of Emissions of Gases and Aerosols from Nature version 2 (MEGAN2, Guenther
132 et al., 2006). Dust and sea salt emissions were also calculated online using the dynamic GOCART
133 dust emissions scheme (Kim et al., 2017) and sea salt scheme (Gong, 2003), respectively.

134 The meteorological Lateral Boundary Conditions (LBCs) were derived from the Modern
135 Era Retrospective-Analysis for Research and Applications (MERRA, Rienecker et al., 2011). The
136 trace gas LBCs were based on the 6-hour results from the Model for OZone And Related chemical
137 Tracers (MOZART, Emmons et al., 2010). The aerosol LBCs were from the global GOCART
138 simulation with a resolution of 1.25 (longitude) by 1 (latitude) degree (Chin et al., 2007). Three
139 horizontal resolutions varied from 45-km to 5-km with 15-km in between. Terrain-following sixty
140 vertical levels stretched from surface to 20 hPa with the 1st layer height of approximately 40 meters
141 from surface. The simulation started on December 20, 2009, and ended on December 31, 2010,
142 with the first 11 days as the spin-up.

143

144 3. Results

145 3.1. Comparisons with observations

146 The NU-WRF results out of different horizontal resolutions have compared with ground
147 observations using the following statistic measures:

148 Correlation coefficient:
$$r = \frac{\sum_{i=1}^n (m_i - \bar{m})(o_i - \bar{o})}{\sqrt{\sum_{i=1}^n (m_i - \bar{m})^2} \sqrt{\sum_{i=1}^n (o_i - \bar{o})^2}}$$

149 Mean bias:
$$MB = \frac{1}{n} \sum_{i=1}^n (m_i - o_i)$$

150 Normalized mean bias:
$$NMB = \frac{\sum_{i=1}^n (m_i - o_i)}{\sum_{i=1}^n o_i} \times 100\%$$

151 Root mean square error:
$$RMSE = \sqrt{\frac{\sum_{i=1}^n (m_i - o_i)^2}{n}}$$

152 Normalized standard deviation:
$$NSD = \sqrt{\frac{\frac{\sum_{i=1}^n (m_i - \bar{m})^2}{n-1}}{\frac{\sum_{i=1}^n (o_i - \bar{o})^2}{n-1}}}$$

153 Where, m_i and o_i denote for the modeled and observed values at time-space pair i ; \bar{m} and \bar{o}
154 represent the average modeled and observed values, respectively. r describes the strength and
155 direction of a linear relationship between two variables – a perfect correlation has a value of 1.
156 NMB and MB depict the mean deviation of modeled results from the respective observations. A
157 perfect model simulation yields an NMB and a MB of 0. $RMSE$ measures the absolute accuracy of
158 a model prediction. The smaller the $RMSE$, the better the model performance is. Similar to NMB



159 and *MB*, a *RMSE* of 0 indicates a perfect model prediction. *NSD* is a measure to check how well
160 the model can reproduce the variations of observations – a value of 1 represents a perfect
161 reproduction of observed variations.

162

163 3.1.1. Meteorology

164 The 2010 meteorological observations were collected at the standard stations operated by
165 China Meteorological Administration (CMA, <http://data.cma.cn/en>). The locations of each site
166 within our study domain were represented with the black dots in Figure 1. In total there were 77
167 sites reporting daily average values of wind speed (Wind), air temperature (Temp), and relative
168 humidity (RH), as well as daily total precipitation (Precip). Figure 2 (top row) shows the Taylor
169 diagram summarizing *r*, *NMB*, and *NSD* of the comparison of regional mean (average of
170 observations from 77 sites) daily meteorological variables. Along the azimuthal angle is *r*. *NSD*
171 is proportional to the radial distance from the origin. *NMB* (sign and range) are represented by
172 geometric shapes. The statistical measures under 45-, 15-, and 5-km resolutions are represented by
173 color blue, green, and red, respectively. The closer to the point “Obs” on the Taylor diagram and
174 smaller of *NMB*, the better the model performance is.

175 It can be seen that the model horizontal resolution has little impact on surface air
176 temperature simulation. Regardless of resolution selections, the modeled temperature correlated
177 very well with the corresponding observations with *r* values all approaching 0.99. NU-WRF also
178 reproduced the observed temperature variations well with *NSD* ranging between 1.05 and 1.10.
179 Meanwhile, *NMB* was within $\pm 1\%$ for all experimented resolutions. *RMSEs* were 1.13 K, 2.26 K,
180 and 2.02 K for the 45-km, 15-km, and 5-km grids, respectively. The insensitivity of surface air
181 temperature to the choice of model resolutions was also reported by Gao et al. (2017), who used
182 WRF to explore the issue for summer seasons at the 36-, 12-, and 4-km resolutions.

183 On the other hand, the horizontal resolution has a remarkable effect on surface wind speed
184 as shown in Figure 2 (top row). At 5-km resolution, NU-WRF yielded a *r* value of 0.75, *NMB* of
185 approximately 54%, and *NSD* of 1.78. NU-WRF simulated a large variation in wind than the
186 observed ones. As comparisons, the values of *r*, *NMB*, and *NSD* for 15-km and 45-km were 0.54,
187 95%, 2.14, and 0.71, 103%, 2.01, respectively. The respective *RMSEs* out of the 45-km, 15-km,
188 and 5-km grids were 2.87, 2.82, and 1.67 m s⁻¹. It was apparent that 5-km resolution gave the
189 overall best wind speed simulation compared to the observations, though NU-WRF overestimated
190 the surface wind speed in all cases. The wind speed overestimate, especially under low wind
191 conditions, was a common problem in all MICS-Asia participating models and other weather
192 forecast models (Gao et al., 2018). This overestimate stemmed from many factors, including but
193 not limited to terrain data uncertainty, poor representation of urban surface effect, horizontal and
194 vertical grid resolutions, etc. Dr. Yu (2014) in her doctoral dissertation pointed out that surface
195 wind simulation would be improved upon using more accurate land-use data. This is expected
196 since surface wind is largely dependent on the land surface characteristics, such as albedo and
197 roughness. High-resolution grid tends to have more accurate land-use representation seeing the
198 inhomogeneous nature of land type.

199 NU-WRF simulations at all three resolutions yielded the similar reproductions of the
200 observed variations in relative humidity (RH) with the *NSD* ranging between 0.87 and 0.88. The
201 modeled RH was less variable than the observed one. While the modeled RH at 45-km resolution
202 (*r* = 0.84) better correlated with the observations than those at the finer resolutions did
203 (approximately 0.67 for both 15-km and 5-km resolutions), the *NMB* at this resolution was the
204 largest (-17%) among the three cases. The *NMBs* for 15-km and 5-km cases were -10% and -12%,



205 respectively. Overall, NU-WRF underestimated the surface RH. The respective *RMSEs* for 45-km,
206 15-km, and 5-km resolutions were 13.2%, 12.6%, and 13.3%. The simulation with the 15-km grid
207 appeared to yield the overall best RH in three cases.

208 It was interesting to find that NU-WRF simulated the best precipitation, as directly
209 compared to the rain gauge data, when using the 45-km grid. At this resolution, NU-WRF gave *r*
210 of 0.81, *NMB* of 1.7%, *RMSE* of 3.2 mm day⁻¹, and *NSD* of 1.41. As comparisons, the values of *r*,
211 *NMB*, *RMSE*, and *NSD* for 15-km and 5-km were 0.53, 76%, 5.7 mm day⁻¹, 1.71, and 0.52, 80%,
212 5.8 mm day⁻¹, 1.72, respectively. Finer resolutions indeed yielded worse results in precipitation
213 modeling as compared to the site data. This may be because precipitation was a very heterogeneous
214 phenomenon – finer model grid had larger chances to miss a precipitation event or hit an event
215 that was not existent, leading to greater overall bias and poorer correlation. On the contrary, Gao
216 et al. (2017) compared their WRF modeled results to the gridded precipitation based on daily rain
217 gauge data that were gridded to the 0.125° resolution using the synergraphic mapping algorithm
218 with topographic adjustment to the monthly precipitation climatology (Maurer et al., 2004). They
219 reported that the modeled precipitation out of the 4-km resolution was much improved over that
220 out of the coarser 36- or 12-km resolutions.

221

222 3.1.2. Air quality

223 The difference seen in the aforementioned meteorology would cause varied performances
224 on air quality simulations at various model horizontal resolutions. In this study, the NU-WRF
225 simulated surface air quality was compared to the corresponding observations. The 2010 ground-
226 level air quality data were obtained from the Chinese Ecosystem Research Network (CERN,
227 <http://www.cern.ac.cn>) operated by the Institute of Atmospheric Physics of Chinese Academy of
228 Sciences. There were 25 monitoring sites distributed within a 500 km by 500 km area centering
229 around Beijing, China (open diamond in Figure 1). The site locations and characteristics were
230 listed in Table 1. 22 out of 25 sites were either in an urban or a suburban setting, with the balance
231 being in a rural setting. Each site reported hourly concentrations of at least one of the following
232 six pollutants – ozone (O₃), nitrogen oxides (NO_x), carbon monoxide (CO), sulfur dioxide (SO₂),
233 and particulate matters with aerodynamic diameters less than 2.5 and 10 μm (PM_{2.5} and PM₁₀).

234

235 a. Regional average

236 First, the regional mean (averaged across 25 sites) daily surface concentrations from both
237 observations and simulations, paired in space and time, were calculated. The *r*, *NME*, and *NSD*
238 were then computed and illustrated in a Taylor diagram (Figure 2 (bottom row)).

239 The six pollutants can be put into two groups – one most relevant to ozone photochemistry
240 including O₃, NO_x, and CO, and the other closely tied to aerosols including SO₂, PM_{2.5}, and
241 PM₁₀. It was readily seen that the *r* values of O₃, NO_x, and CO were not very sensitive to the
242 choice of model horizontal resolutions. For O₃, the *r* values for 45-km, 15-km, and 5-km grids
243 were all around 0.85. The respective *r* values were 0.84, 0.81, 0.80 for NO_x, and 0.80, 0.75, 0.73
244 for CO. In general, however, NU-WRF reproduced the observed variations in O₃, NO_x, and CO
245 better with a fine resolution than with a coarse one. *NSD* of 1.23 for O₃ at 5-km resolution was the
246 closest to 1 among three resolutions (1.24 for 15-km and 2.01 for 45-km). *NSDs* were 0.40, 0.36,
247 0.46 for NO_x, and 0.24, 0.27, 0.31 for CO, under the 45-km, 15-km, and 5-km resolutions,
248 respectively, suggesting that simulations with the finest resolution tended to reproduce the
249 observed variations better than the ones with coarse resolutions for these three trace gases.
250 Meanwhile, NU-WRF yielded the smallest bias when employing the fine resolution grid. *NMBs*



251 for O₃ decreased from 115% to 92% when grid resolutions increased from 45-km to 5-km. *NMBs*
252 were -38%, -30%, -18% for NO_x, and -61%, -55%, -51% for CO, under the 45-km, 15-km, and 5-
253 km resolutions, respectively. It was apparent that NU-WRF overestimated surface O₃ but
254 underestimated NO_x and CO, consistent with the findings in the companion MICS-Asia III studies
255 that based their results on ensemble model simulations (Li et al., 2019; Kong et al., 2019). The
256 majority of the air quality monitoring sites used in this study were in an urban setting, which
257 typically were in a VOC-limited regime. This meant that the underestimate of NO_x would reduce
258 the titration that consumed surface O₃ leading to its overestimate. We further analyzed the model
259 bias for daytime (8-18 local standard time) vs. nighttime. It was found that the nighttime biases for
260 surface O₃ and NO_x were approximately 2~4 times higher than those of daytime, consistent with
261 the finding that insufficient NO_x titration caused overestimate of modeled surface O₃. In the future,
262 improvement of the emissions inventory accuracy and more realistic temporal emissions
263 distribution may help improving NU-WRF performance in simulating O₃ photochemistry.

264 NU-WRF simulated less variations in 3 aerosol related pollutants than those of
265 observations under all applied horizontal resolutions. The *NSDs* ranged from 0.56 (for SO₂ at 15-
266 km resolution) to 0.96 (for PM_{2.5} at 45-km resolution). Though it reproduced the observed SO₂
267 variations the best (*NSD* = 0.68) with 5-km resolution, NU-WRF yielded the best *NSD* for PM_{2.5}
268 (0.96) and PM₁₀ (0.92) when 45-km resolution was employed. Similar to 3 trace gases relevant to
269 surface O₃ formation, the choice of model resolution had a limited effect on *r* statistics. The *r*
270 values varied from 0.70 (45-km resolution) to 0.76 (both 15- and 5-km) for surface SO₂, and from
271 0.68 (45-km resolution) to 0.63 (5-km) for PM_{2.5}. The *r* values for PM₁₀ were all around 0.58
272 under the selected resolutions. The impact of model resolution on *NMBs* showed mixed
273 information – while the smallest *NMBs* for SO₂ (20%) and PM₁₀ (-19%) were achieved using the
274 45-km resolution, the smallest *NMB* for PM_{2.5} (1.5%) was observed at the 15-km resolution. The
275 model underestimate of PM₁₀ was consistent with the findings of the companion investigation
276 using the multi-model ensemble analysis (Chen et al., 2019).

277

278 **b. Individual site**

279 The daily average concentrations of each pollutants were calculated and paired in space
280 and time at each air quality monitoring site. Then the statistics at each individual site was computed.

281 Figure 3 illustrates the comparisons of *MB*, *RMSE*, and correlation coefficient (*r*) of surface
282 O₃ from different horizontal resolutions at each site. It can be found that there was no single
283 resolution that yielded the best correlation across all sites. For example, the simulation with the
284 45-km horizontal resolution gave the best correlation over sites BD, CFD, CZ, HJ, SJZ, SQL, TG,
285 TJ, TS, XH, XL, YF, YJ, and ZJK. On the other end of spectrum, BJT, DT, and LTH achieved the
286 best correlation when the 5-km grid was applied. QHD saw the best correlation out of the
287 simulation with the 15-km resolution. In any cases, however, the variations of *r* values from
288 different horizontal resolutions at each site were small (less than 0.04). On the other hand, NU-
289 WRF yielded the worst *MB* and *RMSE* when employing the 45-km resolution grid, while *MB* and
290 *RMSE* were similar between simulations with 15-km and 5-km resolutions. Typically, at sites with
291 urban/suburban settings, *MB* (*RMSE*) based on the 45-km grid was approximately 15~30%
292 (20~40%) higher than that out of the 15-km or 5-km grids. It appeared that NU-WRF tended to
293 have a better performance on ground-level O₃ simulation when increasing the horizontal resolution
294 from 45-km to 15-km, but further finer resolution had diminished impact on improving surface O₃
295 modeling. This was consistent with the finding by Valari and Menut (2008) who concluded that



296 the benefit of finer horizontal resolution grid to improving surface O₃ forecast skill would diminish
297 at certain point.

298 Figure 4 shows the PM_{2.5} case of comparisons of *MB*, *RMSE*, and *r*. Only 10 sites reported
299 PM_{2.5} measurements over year 2010. In general, the NU-WRF simulation with the 45-km grid
300 correlated better to the respective observations than the other 2 resolutions. The only exception
301 was site BD that saw the best correlation for the 5-km resolution. *MB* and *RMSE* results were
302 mixed with no single resolution giving superior results across all sites. Over 2 rural sites (LS and
303 XL), the simulations with the 15-km or 5-km grids yielded remarkably smaller *MB* but correlated
304 less to the corresponding observations than the one with the 45-km grid. Over 8 urban/suburban
305 sites, BD, SQL, and TG experienced the smallest *MB* when employing the 5-km resolution grid,
306 while TG, TJ, and XH saw the least bias at the 45-km resolution. The smallest *MB* at BJT and
307 LTH occurred using the 15-km grid.

308 At the individual site level, the impact of grid resolution on surface NO_x and CO (figures
309 not shown) modeling was similar to that at the regional average. Finer resolution simulation
310 generally reduced *MB* and *RMSE*. The results out of the 45-km grid always had the largest bias.
311 The underestimates of NO_x at least partially explained the overestimate of surface O₃ at each site
312 due to a less efficient NO-titration of O₃. This suggested that a higher resolution modeling with
313 more accurate spatial representation of NO_x emissions would help improving its performance on
314 surface O₃ simulations.

315 The signals for SO₂ and PM₁₀ (figures not shown) simulations were mixed as well. For
316 example, the largest bias for SO₂ simulation over sites BD, CZ, GA, HS, LS, QA, QHD, XH, XL,
317 YF, and YJ occurred when applying the 45-km grid, while the maximum bias over BJT, DT, HJ,
318 LF, LTH, SJZ, SQL, TG, TJ, TS, ZJK, and ZZ happened at the 5-km resolution. Sites CD and
319 CFD saw the largest bias at the 15-km resolution. Unlike PM₁₀ that was almost always
320 underestimated at each site regardless of grid resolutions, SO₂ was overestimated at 18 out of 25
321 sites and underestimated at the remaining 7 sites.

322

323 *c. Extreme values*

324 High concentrations of air pollutants are of more concerns because of their adverse health
325 effects on both human beings and ecosystem. High pollutant concentrations also pose a greater
326 risk for non-compliance of the ambient air quality standards. Therefore, evaluations of impacts of
327 grid resolution on extreme concentrations of air pollutants are desirable.

328 Figure 5 displays the probability density function distributions of six pollutants based on
329 hourly surface concentrations across the monitoring sites. This analysis was focused on high
330 pollutant concentrations with the cutoff values for CO, O₃, NO_x, SO₂, PM_{2.5}, and PM₁₀ being
331 1.1 ppmv, 60 ppbv, 25 ppbv, 5.5 ppbv, 15 μg m⁻³, and 30 μg m⁻³, respectively. It appeared that
332 NU-WRF, regardless of the grid resolutions, failed to simulate surface CO with concentrations
333 more than 4 ppmv, likely due to the underestimate of CO emissions (Kong et al., 2019). The grid
334 resolution appeared to have limited impacts on surface PM₁₀ simulations when its concentrations
335 were more than 200 μg m⁻³. On the other hand, the grid resolution showed large impacts on NU-
336 WRF's capability in simulating high surface concentrations of O₃, NO_x, SO₂, and PM_{2.5}. For
337 surface O₃ with concentrations more than 100 ppbv, the NU-WRF results with the 45-km grid
338 appeared to better agree with the probability distribution of observations. For surface NO_x with
339 concentrations more than 70 ppbv, the NU-WRF results with the 5-km resolution grid better
340 mimicked the observed distribution. Modeling with the 5-km grid also yielded the best results of



341 distributions, in comparisons to the respective observations, of SO₂ with concentrations more than
342 45 ppbv, and of PM_{2.5} with concentrations greater than 120 µg m⁻³.

343 Table 2 lists the occurrences of violations of China's national ambient air quality standards
344 (NAAQS) for the six pollutants from both observations and simulations. It was apparent that NU-
345 WRF failed to report CO violations at any grid resolutions. No CO NAAQS violation was
346 simulated but the observation showed that surface CO exceeded the national standard by more
347 than 1000 times. NU-WRF underestimated the NAAQS exceedances of NO_x and SO₂. A higher-
348 resolution grid appeared to be able to catch more violations although the modeled results at the 5-
349 km resolution only captured 33% and 10% observed exceedances of NO_x and SO₂, respectively.
350 NU-WRF overestimated surface O₃ and PM_{2.5} when their concentrations were more than the
351 corresponding NAAQS. The fine grid resolution (i.e., 5-km) appeared to reduce the overestimation
352 of surface O₃ exceedances largely as compared to the 45-km grid but only marginally compared
353 with the 15-km grid. Compared to the observed occurrences of surface O₃ standard violation
354 (3,684), the simulated exceedances were 6.7, 2.8, and 2.7 times higher when employing the 45-
355 km, 15-km, and 5-km resolution grid, respectively. The observations showed 1,343 occurrences
356 of surface PM_{2.5} exceedances, while the modeled exceedances were 377, 267, and 231 more for
357 the 45-km, 15-km, and 5-km grids, respectively. As for surface PM₁₀, the modeled exceedances
358 were approximately 27%, 43%, and 41% less than the observed one for the 45-km, 15-km, and 5-
359 km grids, respectively.

360

361 **3.2. Inter-resolution comparisons**

362 It is informative to compare the NU-WRF results out of different horizontal resolutions.
363 This can help understand the reasons why model resolution matters.

364

365 **3.2.1. Emissions**

366 There were two types of emissions applied in this study. One was the prescribed emissions
367 out of the anthropogenic and wild fire sources, and the other was emissions computed online using
368 the real-time meteorology (or dynamic emissions) including emissions from biogenic sources, dust
369 sources, and sea spray. Amounts and temporal variations of dynamic emissions depended on
370 surrounding environmental conditions. For example, air temperature and solar radiation regulates
371 biogenic emissions (Guenther et al., 2006). Surface wind speed plays a major role in both dust
372 (Ginoux et al., 2001; Chin et al., 2002) and sea salt emissions (Gong, 2003).

373 For the prescribed emissions, the differences of domain total masses out of each grid were
374 small (less than 5%). However, the emission gradient around sources of a fine resolution grid
375 appeared to be sharper than that of a coarse resolution grid. This meant that a coarse grid tended
376 to distribute the prescribed emissions more evenly into the domain, while a fine grid tended to
377 produce more extreme concentrations of primary pollutants (emitted directly from a source) such
378 as NO_x and SO₂, as shown in Table 2.

379 Online calculated emissions, on the other hand, displayed large differences in both gradient
380 and total mass. Similar to the case of prescribed emissions, a fine resolution grid tended to give a
381 sharper gradient of dynamic emissions than a coarse resolution grid did, as highlighted in Figure
382 6 (1st row) that illustrated the biogenic isoprene emissions (mol km⁻² hr⁻¹) on a typical summer day.
383 It was apparent that much more details were simulated using a fine resolution grid - the flow of
384 Yellow River can even be seen on the 5-km resolution map that was otherwise invisible from the
385 coarser resolution maps. Meanwhile, the total masses of dynamic emissions showed large
386 difference out of different resolution grids as listed in Table 3. On an annual basis, the domain



387 total isoprene emissions were 740,562 tons when estimated using the 45-km grid, approximately
388 85% and 86% of those with the 15-km and 5-km grids, respectively. The total dust emissions out
389 of the 45-km grid were 2,431 tons, only 54% and 62% of those based on the respective 15-km and
390 5-km grids. The percentage contrasts for sea salt emissions were even larger with emissions out of
391 the 15-km and 5-km grids being 1.3 and 1.6 times more than those of the 45-km grid, respectively.
392 It should be noted that although they differed greatly between out of the 45-km and 15-km grids,
393 the dynamic emissions out of the 5-km grid were much closer to those out of the 15-km grid,
394 partially explaining why the impact of model resolution on surface air quality was less remarkable
395 by increasing the resolution from 15-km to 5-km than from 45-km to 15-km.

396 The spatial (gradient) and mass variations in emissions out of different resolution grids
397 would result in difference in air quality simulations.

398

399 **3.2.2. Meteorology**

400 It's been reported that simulated meteorology varies in response to selections of model grid
401 resolutions (e.g., Tie et al., 2010; Lee et al., 2018). Meteorology plays an important role in
402 regulating regional air quality – it affects emissions amount originating from biogenic, dust, and
403 sea sources; it impacts atmospheric chemical and photochemical transformation; and it directs air
404 flows and the associated transport of trace gases and aerosols. In this investigation, a few
405 meteorological parameters key to air pollutant generation and accumulation were analyzed,
406 including surface wind, air temperature, downward shortwave flux at surface (SWDOWN),
407 planetary boundary layer height (PBLH), and cloud water (liquid + ice) path (CWP). We focused
408 on months that were prone to deteriorated PM_{2.5} (January) and O₃ (July) air quality as shown in
409 Figure 6 and Table 3.

410 NU-WRF simulated a similar direction of surface wind in July 2010 over the eastern
411 portion of the domain (2nd row of Figure 6). In general, average wind speed was larger over Bohai
412 Sea and Yellow Sea than over the surrounding land areas with dominating wind direction being
413 south and southeast. Based on the results from the 15-km and 5-km grids, the peak average wind
414 speeds over 4 m s⁻¹ were found in Bohai Bay blowing to Tianjin and Beijing. However, such a
415 peak was absent from the 45-km grid simulation. In the west portion of the domain, the wind
416 direction changed from southeast in the south to southwest in the north in general. Compared to
417 the more organized wind directions out of the 45-km grid, wind directions out of the 15- and 5-km
418 grids were more chaotic. Averaged over the domain, the January mean wind speed out of the 45-
419 km grid was 2.92 m s⁻¹, which were 7% and 16% larger than those of the 15-km and 5-km grids,
420 respectively. The largest July mean wind speed was again simulated with the 45-km grid, 10% and
421 12% larger than the corresponding wind speed out of the 15-km and 5-km grids, respectively.

422 Overall, NU-WRF simulated very similar magnitudes and spatial patterns of surface air
423 temperature in July (3rd row of Figure 6), regardless of the selections of grid resolutions. Large
424 portions of the NCP experienced more than 300 K of July average air temperature. The minimum
425 average temperature of approximately 290 K was found in the central north part of the domain,
426 which was part of the Mongolian Plateau with the elevation being over 1,500 m above the sea level.
427 The domain average January and July surface air temperature were around 268 K and 300 K,
428 respectively, for simulations out of all three grids.

429 As expected, the modeling results from all three grids (4th row of Figure 6) showed that
430 July average PBLH over sea was much smaller than that over land. The maximum average PBLH
431 (more than 1,000 m) was found in the northwest portion of the domain, also in the Mongolian
432 Plateau with a dominant land cover type of grass. The largest domain-average PBLHs in January



433 and July were found from the simulations out of the 15-km and 45-km grids, respectively. In
434 January, the differences of the domain-average PBLHs from different grid resolutions were small
435 and within 2%. In July, however, such difference can be over 9%.

436 Regardless of the grid resolutions, NU-WRF simulated a generally southeast-northwest
437 gradient of SWDOWN in July with the highest flux (over 300 W m^{-2}) occurring in the northwestern
438 domain (5th row of Figure 6). The differences between the maximum and minimum domain
439 average SWDOWN out of 3 grids were 5.6% and 3.3% in January and July, respectively.

440 CWP represented the vertical integration of cloud water (including both liquid and ice
441 phases) contents and can be regarded as a proxy of cloud amount and coverage. Opposite to the
442 SWDOWN case, NU-WRF modeled a generally northwest-southeast gradient of CWP in July with
443 the high values found in the southeastern domain (6th row of Figure 6). This was understandable
444 since cloud reflects and scatters the incoming solar radiation and thus affect SWDOWN. Large
445 cloud existence tended to reduce the solar flux reaching the underneath Earth surface. The CWP
446 differences among the model results out of different grid resolutions appeared to be larger than
447 SWDOWN differences. In July, the domain average CWPs out of the 15-km and 5-km grids were
448 37% and 33% larger than that of the 45-km grid, respectively. The gaps were even larger in January,
449 during which the domain average CWPs from the 15-km and 5-km grids were approximately 1.6
450 times larger than that from the 45-km grid.

451

452 3.2.3. Air Quality

453 In response to the aforementioned emissions and meteorological variations resulted from
454 the selections of model grid resolutions, changes in regional air quality ensued as illustrated in
455 Figure 7 and Table 3. This figure shows the July average concentrations of ground-level O_3 and
456 its precursors of NO_x and CO , as well as the January mean concentrations of surface SO_2 , $\text{PM}_{2.5}$,
457 and PM_{10} , during which month the respective pollutants tended to reach high concentrations.

458 O_3 is a secondary pollutant that is formed in the atmosphere through complex
459 photochemical processes upon existences of its precursors such as NO_x and volatile organic
460 compounds (VOC). Figure 7 (row 1) shows that the spatial distributions of surface O_3 are similar
461 to each other but the concentrations out of the 15-km and 5-km grids are smaller than those from
462 the 45-km grid. The domain average surface O_3 concentration in July was approximately 87 ppbv
463 based on the results from the 45-km grid, 26% and 25% higher than those out of the 15-km and 5-
464 km grid, respectively. In January, however, the highest domain average concentration occurred
465 when the 5-km grid was used, which was 5.3% higher than that out of the 45-km grid.

466 For the primary pollutants, i.e., NO_x , CO , and SO_2 (rows 2-4 of Figure 7, respectively),
467 which were emitted directly by their sources, the spatial distributions of their concentrations
468 mimicked closely with their emission distributions. High concentrations centered around emission
469 sources with a reducing gradient outward. The domain average concentrations of these 3 pollutants
470 out of the 45-km grid results were always the largest in both January and July. The average surface
471 NO_x concentrations from the simulations out of the 15-km and 5-km grids were around 24% lower
472 than their counterparts out of the 45-km grid in January. In July, the differences were reduced to
473 7.9% and 11.8% for the 15-km and 5-km grids, respectively. On the other hand, the larger
474 percentage differences, as compared to the results out of the 45-km grid, occurred in July than in
475 January for both CO and SO_2 . For example, the surface CO concentrations out of the 5-km grid
476 were 12.3% and 30.6% lower than those based on the 45-km grid in January and July, respectively.
477 The respective ground-level SO_2 concentrations from the 5-km grid were 20.5% and 38.9% lower
478 than those from the 45-km grid in January and July.



479 It was interesting to note that among the 3 cases, the domain average July surface O₃ and
480 NO_x concentrations were both the highest out of the 45-km grid, contrary to the results discussed
481 in section 3.1.2a where the highest O₃ concentration occurred out of the simulation using the 45-
482 km grid while the highest NO_x concentration happened with the 5-km grid. This seemingly
483 contradicting result was internally consistent. Section 3.1.2a actually depicted the average surface
484 concentrations in an urban environment (23 of 25 monitoring sites were in an urban/suburban
485 setting), where surface O₃ formation was typically VOC controlled such that NO tended to
486 consume O₃ through titrations. As discussed in section 3.2.1, a 5-km grid gave a much sharper
487 emissions gradient with anthropogenic emissions concentrating in urban/suburban areas. This led
488 to higher NO_x concentrations around urban/suburban areas out of the simulation with the 5-km
489 grid, which effectively resulted in lower O₃ concentrations there through the NO titration effect.
490 The domain average discussed in this section, however, was the average covering the vast rural
491 area that generally was NO_x-limited such that surface O₃ formation was controlled by the
492 availability of NO_x – more NO_x resulting in more O₃ through photochemical processes. In this
493 case, the 45-km grid tended to distribute NO_x emissions more evenly in the region, effectively
494 decreasing the surface NO_x concentration in urban areas but increasing it over rural areas. This in
495 turn increased the domain average surface O₃ concentration via photochemistry based on the 45-
496 km resolution results. In addition, the higher air temperature and stronger SWDOWN in July out
497 of the 45-km grid as compared to other two resolutions favored more surface O₃ generations.

498 Vertical distributions of O₃ tend to have a sizable impact on next day's surface O₃ levels
499 (e.g., Kuang et al., 2011; Caputi et al., 2019). Figure 8 illustrates the domain average profiles of
500 vertical wind, NO_x, O₃ (panels a~c), and the average diurnal distribution of surface O₃ (panel d)
501 over July. Here we limited our discussion on the results from the 15- and 5-km grids since 45-km
502 grid artificially allowed more NO_x emissions spreading to rural areas to produce much more O₃
503 as shown in the previous paragraph. Lee et al. (2018) claimed that a coarse resolution model
504 appeared to lower updraft as compared with a fine resolution modeling. This study agreed with
505 their finding as illustrated in Figure 8 (panel a). The domain average July vertical wind out of the
506 simulation with the 5-km grid ranged from 0.25 to 0.45 cm s⁻¹ (upward) between 800 hPa and 400
507 hPa, stronger than the corresponding one out of the 15-km grid. The reason was complex and the
508 aerosol-cloud interaction induced freezing/evaporation-related invigoration mechanism played a
509 role (Lee et al., 2018). The stronger upward wind tended to lift more gaseous pollutants up to the
510 free troposphere as shown in Figure 8 (panel b (NO_x) and c (O₃)). The pollutants there would have
511 visible impacts on the following-day surface air quality, especially on O₃ levels at night and in the
512 morning when sun breaks out the nocturnal planetary boundary layer, as evidenced in Figure 8
513 (panel d). At night with no photochemical formation, surface O₃ concentration was largely
514 controlled by upper-level O₃ mixing down, NO titration and O₃ dry deposition. With the virtually
515 same average surface NO concentrations out of the 15- and 5-km grids, the upper-level O₃ mixing
516 down appeared to control the relative magnitudes of surface O₃ concentrations simulated using the
517 15- and 5-km grids. This partially explained why, at night and early morning, the ground level O₃
518 concentrations were higher out of the 5-km grid than from the 15-km grid. During daytime when
519 the photochemical formation of O₃ takes control, the regional average surface O₃ concentrations
520 is largely determined by the availability of O₃ precursors (i.e., NO_x and VOC) and ambient
521 environmental conditions. In this case, more spreading NO_x emissions out of the 15-km grid
522 appeared to generate more surface O₃ than the 5-km grid did.

523 PM_{2.5} and PM₁₀ were mixed pollutants that not only were emitted by various sources but
524 also were generated in the atmosphere through physical and chemical processes. Figure 7 shows



525 that high surface concentrations of PM_{2.5} (more than 120 $\mu\text{g m}^{-3}$, row 5) and of PM₁₀ (more than
526 170 $\mu\text{g m}^{-3}$, row 6) were still found around the source areas based on the modeling results out of
527 the 15-km and 5-km grids. However, high PM_{2.5} and PM₁₀ concentrations spread out to larger
528 areas based on the results from the 45-km grid as compared to the ones from the finer grid
529 resolutions. Similar to the primary pollutants, the largest domain average surface concentrations
530 occurred when a 45-km grid was used for the NU-WRF simulation. The domain average PM_{2.5}
531 concentrations out of the 15-km and 5-km grids in January were 15.7% and 14% lower than those
532 from the 45-km grid, respectively. The surface PM_{2.5} concentration differences among results out
533 of different grid resolutions grew larger in July, reaching 48% when comparing the result from the
534 5-km grid to that from the 45-km grid. The domain average surface PM₁₀ concentrations showed
535 similar pattern to that of PM_{2.5} with the results out of the 5-km grid being 12.2% and 44.2%
536 smaller than that from the 45-km grid.

537 It is worth noting that the magnitudes and spatial distributions of ground-level pollutants
538 were close to each other between the results out of the 15-km and 5-km grids. This again indicates
539 that the improvement of fine grid resolution modeling reduces at a certain point. In future MICS-
540 Asia efforts, a 15-km grid appears to offer the optimized results balanced with performance and
541 resources.

542

543 4. Summary

544 Contributing to MICS-Asia Phase III whose goals included identifying and reducing air
545 quality modeling uncertainty over the region, this investigation examined the impact of model grid
546 resolutions on the performances of meteorology and air quality simulation. To achieve this, NU-
547 WRF was employed to simulate 2010 air quality over the NCP region with three grid resolutions
548 of 45-km, 15-km, and 5-km. The modeling results were compared to the observations of surface
549 meteorology archived by CMA, and of ground-level air quality collected in CERN. The inter-
550 model comparison among the simulation results out of three grids were also conducted to
551 understand the reasons why model resolution mattered.

552 The analysis showed that there was no single resolution which would yield the best
553 reproduction of meteorology and air quality across all monitoring sites. From a regional average
554 perspective (i.e., across all monitoring sites in this study), the choice of grid resolution appeared
555 to have a minimum influence on air temperature modeling but affected wind, RH, and precipitation
556 simulation profoundly. A 5-km grid appeared to give the best wind simulation as compared to the
557 observations quantified by bias, RMSE, standard deviation, and correlation. Compared to one
558 using the 45-km grid, the simulated wind speed from a 5-km grid reduced the positive bias by
559 46.8%. While a 15-km grid yielded the best overall performance on RH modeling, the result out
560 of the 45-km grid gave the most realistic reproduction of precipitation. The statement on
561 precipitation should be taken with caution since it was based on the comparison with the site
562 observations. Seeing the very heterogeneous nature of precipitation, the penalty of model hitting
563 or missing a rain event was severe. Thus, the coarse grid covering more areas within a grid cell
564 would reduce chances of mistaken precipitation hitting or missing simulations. However, a
565 comparison of modeled precipitations to gridded “observation” that was re-constructed using the
566 synergraphic mapping algorithm with topographic adjustment to the monthly precipitation
567 climatology showed opposite result, where the fine resolution modeling showed superior
568 reproduction of precipitation than the coarse resolution simulation (Gao et al., 2017).

569 The simulated meteorology differences due to the selection of grid resolutions would
570 consequently lead to differences in air quality simulation. Air pollutant concentrations were



571 basically determined by their emissions and underlying meteorology that directed their formation
572 (e.g., O₃ and aerosols), transport, and removal processes. For the prescribed emissions originated
573 from anthropogenic and wild fire sources, the grid resolution had limited influence on emission
574 amount – less than 5% difference with each other under the different resolution grids - but large
575 impact on emission spatial distribution with sharper emission gradient around sources out of a fine
576 resolution grid than from a coarse resolution one. For the dynamic emissions driven by
577 meteorology, not only was an emission gradient around a source larger out of a higher resolution
578 grid, but also the total emission amount varied greatly. For example, the domain total annual
579 biogenic isoprene emissions from a 5-km grid was about 16% larger than those out of a 45-km
580 grid due to the underlying differences in land cover and meteorology.

581 Though the impact of grid resolution on air quality varied from location to location, finer
582 grid yielded better results for daily mean surface O₃, NO_x, CO, and PM_{2.5} simulations from a
583 regional average perspective. For example, after reducing the grid resolution from 45-km to 15-
584 km, the positive bias of daily mean surface O₃ and PM_{2.5} decreased by 15% and 75%, respectively.
585 Fine resolution modeling was especially beneficial to high pollutant concentration forecast. This
586 was important to air quality management. Taking China's NAAQS as cutoff values for each
587 pollutant, the frequencies of noncompliance occurrences of O₃, NO_x, SO₂, and PM_{2.5} out of the
588 5-km grid simulation were much closer to the observations than those out of the 45-km modeling
589 were. It also was worth noting that the benefit of increasing grid resolution to better surface O₃
590 and PM_{2.5} simulations started to diminish when the horizontal resolution reached 15-km, agreeing
591 with the finding by Valari and Menut (2008).

592 It should be pointed out that NU-WRF significantly overestimated surface O₃ concentration
593 but underestimated ground-level CO and NO_x concentrations regardless of grid resolutions. This
594 was true not only on the regional averages but also at majority of the monitoring sites. The missing
595 emissions was believed to be largely responsible for this result (Kong et al., 2019). Underestimate
596 of surface NO_x tended to increase ground-level O₃ due to the reduced titration effect, especially at
597 night.

598 In conclusion, grid resolution had a profound effect on NU-WRF performance on
599 meteorology and air quality over the East Asia. Fine resolution grid did not always generate the
600 best modeling results and the proper selection of horizontal resolution hinged on investigation
601 topics for a given set of physics and chemistry choices in a model. With regard to MICS-Asia
602 Phase III whose major goal was to examine air quality, a 15-km horizontal grid appeared to be an
603 appropriate choice to optimize model performance and resource usage.

604 605 **Competing interests**

606 The authors declare that they have no conflict of interest.

607 608 **Author contribution**

609 ZT and MC designed the experiments. ZT, MG, TK, DK, and HB carried out the
610 experiments working on various modeling components. YW collected, organized, and archived
611 the ground air quality measurement data. All authors contributed to model result analysis and
612 interpretation. ZT prepared the manuscript with contributions from all co-authors.

613 614 **Acknowledgement**

615 This work was supported by the NASA's Atmospheric Composition: Modeling and
616 Analysis Program (ACMAP) and Modeling, Analysis, and Prediction (MAP) program. The



617 authors thank MICS-Asia for its organized platform of discussion and data sharing. This work is
618 not possible without the supercomputing and mass storage support by NASA Center for Climate
619 Simulation (NCCS). All data collected and generated for this research are archived and stored on
620 NCCS servers. Due to the sheer size of data, it is impractical to upload data to a public domain
621 repository. However, the authors will be happy to share data on an individual request basis.
622
623



624 **References**

- 625 Akimoto, H., Mori, Y., Sasaki, K., Nakanishi, H., Ohizumi, T., and Itano, Y.: Analysis of
626 monitoring data of ground-level ozone in Japan for long-term trend during 1990-2010:
627 Causes of temporal and spatial variation, *Atmos. Environ.*, 102, 302-310, 2015.
- 628 Anenberg, S. C., Horowitz, L. W., Tong, D. Q., and West J. J.: An estimate of the global burden
629 of anthropogenic ozone and fine particulate matter on premature human mortality using
630 atmospheric modeling, *Environ. Health Perspect.*, 118(9), 1189-1195,
631 doi:10.1289/ehp.0901220, 2010.
- 632 Cai, W., Li, K., Liao, H., Wang, H., and Wu, L.: Weather conditions conducive to Beijing severe
633 haze more frequent under climate change, *Nature Climate Change*, 7, 257-263,
634 doi:10.1038/NCLIMAE3249, 2017.
- 635 Caputi, D. J., Faloon, I., Trousdell, J., Smoot, J., Falk, N., and Conley, S.: Residual layer ozone,
636 mixing, and the nocturnal jet in California's San Joaquin Valley, *Atmos. Chem. Phys.*, 19,
637 4721-4740, doi:10.5194/acp-19-4721-2019, 2019.
- 638 Carmichael, G., Calori, G., Hayami, H., Uno, I., Cho, S. Y., Engardt, M., Kim, S. B., Ichikawa,
639 Y., Ikeda, Y., Woo, J. H., Ueda, H., and Amann, M.: The MICS-Asia study: model
640 intercomparison of long-range transport and sulfur deposition in East Asia, *Atmos. Environ.*,
641 36, 175-199, 10.1016/s1352-2310(01)00448-4, 2002.
- 642 Carmichael, G., Sakurai, T., Streets, D., Hozumi, Y., Ueda, H., Park, S., Fung, C., Han, Z., Kajino,
643 M., and Engardt, M.: MICS-Asia II: The model intercomparison study for Asia Phase II:
644 methodology and overview of findings, *Atmos. Environ.*, 42, 3468-3490,
645 10.1016/j.atmosenv.2007.04.007, 2008.
- 646 Chen, L., Gao, Y., Zhang, M., Fu, J. S., Zhu, J., Liao, H., Li, J., Huang, K., Ge, B., Wang, X.,
647 LAM, Y. F., Lin, C.-Y., Itahashi, S., Nagashima, T., Kajino, M., Yamaji, K., Wang, Z., and
648 Kurokawa, J.-I.: MICS-Asia III: Multi-model comparison and evaluation of aerosol over East
649 Asia, *Atmos. Chem. Phys. Discuss.*, <http://doi.org/10.5194/acp-2018-1346>, in review, 2019.
- 650 Chin, M., Ginoux, P., Kinne, S., Torres, O., Holben, B. N., Duncan, B. N., Martin, R. V., Logan,
651 J. A., Higurashi, A., and Nakajima, T.: Tropospheric aerosol optical thickness from the
652 GOCART model and comparisons with satellite and Sun photometer measurements, *J.*
653 *Atmos. Sci.*, 59, 461-483, 2002.
- 654 Chin, M., Diehl, T., Ginoux, P., and Malm, W.: Intercontinental transport of pollution and dust
655 aerosols: implications for regional air quality, *Atmos. Chem. Phys.*, 7, 5501-5517,
656 doi:10.5194/acp-7-5501-2007, 2007.
- 657 Chou, M.-D. and Suarez, M. J.: A solar radiation parameterization (CLIRAD-SW) for atmospheric
658 studies, NASA Tech. Rep. NASA/TM-1999-10460, vol. 15, 38 pp, 1999.
- 659 Ek, M. B., Mitchell, K. E., Lin, Y., Rogers, E., Grunmann, P., Koren, V., Gayno, G., and Tarpley,
660 J. D.: Implementation of Noah land surface model advances in the National Centers for
661 Environmental Prediction operational mesoscale Eta Model, *J. Geophys. Res.*, 108, 8851,
662 doi:10.1029/2002JD003296, 2003.
- 663 Emmons, L. K., Walters, S., Hess, P. G., Lamarque, J.-F., Pfister, G. G., Fillmore, D., Granier, C.,
664 Guenther, A., Kinnison, D., Laepple, T., Orlando, J., Tie, X., Tyndall, G., Wiedinmyer, C.,
665 Baughcum, S. L., and Kloster, S.: Description and evaluation of the Model for Ozone and
666 Related chemical Tracers, version 4 (MOZART-4), *Geosci. Model Dev.*, 3, 43-67, 2010.
- 667 Gao, M., Carmichael, G. R., Wang, Y., Saide, P. E., Yu, M., Xin, J., Liu, Z., and Wang, Z.:
668 Modeling study of the 2010 regional haze event in the North China Plain, *Atmos. Chem.*
669 *Phys.*, 16, 1673-1691, doi:10.5194/acp-16-1673-2016, 2016.



- 670 Gao, M., Han, Z., Liu, Z., Li, M., Xin, J., Tao, Z., et al.: Air quality and climate change, Topic 3
671 of the Model Inter-Comparison study for Asia Phase III (MICS-Asia III) – Part 1: Overview
672 and model evaluation, *Atmos. Chem. Phys.*, 18 (7), 4859-4884, doi:10.5194/acp-18-4859-
673 2018, 2018.
- 674 Gao, Y., Leung, L. R., Zhao, C., and Hagos, S.: Sensitivity of U.S. summer precipitation to model
675 resolution and convective parameterizations across gray zone resolution, *J. Geophys. Res.*
676 *Atmos.*, 122, 2,714-2,733, doi:10.1002/2016JD025896, 2017.
- 677 Ginoux, P., Chin, M., Tegen, I., Prospero, J., Holben, B., Dubovik, O., and Lin, S.-J.: Sources and
678 global distributions of dust aerosols simulated with the GOCART model, *J. Geophys. Res.*,
679 106, 20,255-20,273, 2001.
- 680 Gong, S. L.: A parameterization of sea-salt aerosol source function for sub- and super-micron
681 particles, *Glob. Biogeochemical Cycles*, 17, No. 4, 1097, doi: 10.1029/2003GB002079, 2003.
- 682 Grell, G. A. and Devenyi, D.: A generalized approach to parameterizing convection combining
683 ensemble and data assimilation techniques, *Geophys. Res. Lett.*, 29, 1693,
684 doi:10.1029/2002GL015311, 2002.
- 685 Grell, G. A., Peckham, S. E., Schmitz, R., McKeen, S. A., Frost, G., Skamarock W. C., and Eder,
686 B.: Fully coupled “online” chemistry within the WRF model, *Atmos. Environ.*, 39, 6957–
687 6975, 2005.
- 688 Gross, A. and Stockwell, W. R.: Comparison of the EMEP, RADM2 and RACM Mechanisms, *J.*
689 *Atmos. Chem.*, 44, 151-170, 2003.
- 690 Guenther, A, Karl, T., Harley, P., Wiedinmyer, C., Palmer, P. I., and Geron, C.: Estimates of global
691 terrestrial isoprene emissions using MEGAN (Model of Emissions of Gases and Aerosols from
692 Nature), *Atmos. Chem. Phys.*, 6, 3181-3210, 2006.
- 693 Hong, S. Y., Noh, Y., and Dudhia, J.: A new vertical diffusion package with an explicit treatment
694 of entrainment processes, *Mon. Wea. Rev.*, 134, 2318-2341, 2006.
- 695 Huang, R.-J., Zhang, Y., Bozzetti, C., Ho, K.-F., Cao, J.-J., Han, Y., Daellenbach, K. R., Slowik,
696 J. G., Platt, S. M., Canonaco, F., Zotter, P., Wolf, R., Pieber, S. M., Bruns, E. A., Crippa, M.,
697 Ciarelli, G., Piazzalunga, A., Schwikowski, M., Abbaszade, G., Schnelle-Kreis, J.,
698 Zimmermann, R., An, Z., Szidat, S., Baltensperger, U., Haddad, I. E., and Prevot, A. S. H.:
699 High secondary aerosol contribution to particulate pollution during haze events in China,
700 *Nature*, 514, 218-222, doi:10.1038/nature13774, 2014.
- 701 Jin, Y., Andersson, H., and Zhang, S.: Air pollution control policies in China: A retrospective and
702 prospects, *Int. J. Environ. Res. Public Health*, 13(12), 1219, doi:10.3390/ijerph13121219,
703 2016.
- 704 Kim, D., Chin, M., Kemp, E. M., Tao, Z., Peters-Lidard, C. D., and Ginoux, P.: Development of
705 high-resolution dynamic dust source function – A case study with a strong dust storm in a
706 regional model, *Atmos. Environ.*, 159, 11-25, doi:10.1016/j.atmosenv.2017.03.045, 2017.
- 707 Kong, L., Tang, X., Zhu, J., Wang, Z., Fu, J. S., Wang, X., Itahashi, S., Yamaji, K., Nagashima,
708 T., Lee, H.-J., Kim, C.-H., Lin, C.-Y., Chen, L., Zhang, M., Tao, Z., Li, J., Kajino, M., Liao,
709 H., Sudo, K., Wang, Y., Pan, Y., Tang, G., Li, M., Wu, Q., Ge, B., and Carmichael, G. R.:
710 Evaluation and uncertainty investigation of the NO₂, C and NH₃ modeling over China under
711 the framework of MICS-Asia III, *Atmos. Chem. Phys. Discuss.*, [http://doi.org/10.5194/acp-](http://doi.org/10.5194/acp-2018-1158)
712 [2018-1158](http://doi.org/10.5194/acp-2018-1158), in review, 2019.
- 713 Krotkov, N. A., McLinden, C. A., Li, C., Lamsal, L. N., Celarier, E. A., Marchenko, S. V., Swartz,
714 W. H., Bucsela, E. J., Joiner, J., Duncan, B. N., Boersma, K. F., Veeffkind, J. P., Levelt, P.
715 F., Fioletov, V. E., Dickerson, R. R., He, H., Lu, Z., and Streets, D. G.: Aura OMI



- 716 observations of regional SO₂ and NO₂ pollution changes from 2005 to 2015, *Atmos. Chem.*
717 *Phys.*, 16(7), 4605–4629, doi:10.5194/acp-16-4605-2016, 2016.
- 718 Kumar, S. V., Peters-Lidard, C. D., Tian, Y., Houser, P. R., Geiger, J. Olden, S., Lighty, L.,
719 Eastman, J. L., Doty, B., Dirmeyer P., Adams, J., Mitchell K., Wood, E. F., and Sheffield, J.:
720 Land Information System – An Interoperable Framework for High Resolution Land Surface
721 Modeling, *Environ. Modelling & Software*, 21, 1,402-1,415, 2006.
- 722 Kuang, S., Newchurch, M. J., Burris, J., Wang, L., Buckley, P. I., Johnson, S., Knupp, K., Huang,
723 G., Phillips, D., and Canrell, W.: Nocturnal ozone enhancement in the lower troposphere
724 observed by lidar, *Atmos. Environ.*, 45, 6078-6084, 2011.
- 725 Lee, S. S. Li, Z., Zhang, Y. Yoo, H., Kim, S., Kim, B.-G., Choi, Y.-S., Mok, J., Um, J., Choi, K.
726 O., and Dong, D.: Effects of model resolution and parameterizations on the simulations of
727 clouds, precipitation, and their interactions with aerosols, *Atmos. Chem. Phys.*, 18, 13–29,
728 doi:10.5194/acp-18-13-2018, 2018.
- 729 Lelieveld, J., Evans, J. S., Fnais, M., Giannadaki D., and Pozzer, A.: The contribution of outdoor
730 air pollution sources to premature mortality on a global scale, *Nature*, 525, 367-371, 2015.
- 731 Li, J., Nagashima, T., Kong, L., Ge., B., Yamaji, K., Fu, J. S., Wang, X., Fan, Q., Itahashi, S., Lee,
732 H.-J., Kim, C.-H., Lin, C.-Y., Zhang, M., Tao, Z., Kajino, M., Liao, H., Li, M., Woo, J.-H.,
733 Kurokawa, J.-I., Wu, Q., Akimoto, H., Carmichael, G. R., and Wang, Z.: Model evaluation
734 and inter-comparison of surface-level ozone and relevant species in East Asia in the context
735 of MICS-Asia phase III, Part I: overview, *Atmos. Chem. Phys. Discuss.*,
736 <http://doi.org/10.5194/acp-2018-1283>, in review, 2019.
- 737 Li, M., Zhang, Q., Kurokawa, J. I., Woo, J. H., He, K., Lu, Z., Ohara, T., Song, Y., Streets, D. G.,
738 Carmichael, G. R., Cheng, Y., Hong, C., Huo, H., Jiang, X., Kang, S., Liu, F., Su, H., and
739 Zheng, B.: MIX: a mosaic Asian anthropogenic emission inventory under the international
740 collaboration framework of the MICS-Asia and HTAP, *Atmos. Chem. Phys.*, 17, 935-963,
741 doi:10.5194/acp-17-935-2017, 2017.
- 742 Lin, M., Holloway, T., Carmichael, G. R., and Fiore, A. M.: Quantifying pollution inflow and
743 outflow over East Asia in spring with regional and global models, *Atmos. Chem. Phys.*, 10,
744 4221-4239, doi: 10.5194/acp-10-4221-2010, 2010.
- 745 Lu, X., Hong, J., Zhang, L., Cooper, O. R., Schultz, M. G., Xu, X., Wang, T., Gao, M., Zhao, Y.,
746 and Zhang, Y.: Severe surface ozone pollution in China: A global perspective, *Environ. Sci.*
747 *Technol. Lett.*, 5, 487-494, 2018.
- 748 Matsui, T., Tao, W.-K., Masunaga, H., Kummerow, C. D., Olson, W. S., Teruyuki, N., Sekiguchi,
749 M., Chou, M., Nakajima, T. Y., Li, X., Chern, J., Shi, J. J., Zeng, X., Posselt, D. J., and
750 Suzuki, K.: Goddard Satellite Data Simulation Unit: Multi-Sensor Satellite Simulators to
751 Support Aerosol- Cloud-Precipitation Satellite Missions, *Eos Trans.*, 90(52), Fall Meet.
752 Suppl., Abstract A21D-0268, 2009.
- 753 Matsui, T., Iguchi, T., Li, X., Han, M., Tao, W.-K., Petersen, W., L'Ecuyer, T., Meneghini, R.,
754 Olson, W., Kummerow, C. D., Hou, A. Y., Schwaller, M. R., Stocker, E. F., and Kwiatkowski,
755 J.: GPM satellite simulator over ground validation sites, *Bull. Am. Meteor. Soc.*, 94, 1653-
756 1660, doi:10.1175/BAMS-D-12-00160.1, 2013.
- 757 Matui, T., Santanello, J., Shi, J. J., Tao, W.-K., Wu, D., Peters-Lidard, C., Kemp, E., Chin, M.,
758 Starr, D., Sekiguchi, M., and Aires, F.: Introducing multi-sensor satellite radiance-based
759 evaluation for regional earth system modeling, *J. Geophys. Res.*, 119, 8450-8475,
760 doi:10.1002/2013JD021424, 2014.
- 761 Maurer, E. P., Wood, A. W., Adam, J. C., Lettenmaier, D. P., and Nijssen, B.: A long-term



- 762 hydrologically based dataset of land surface fluxes and states for the continuous United State,
763 *J. Clim.*, 15(22), 3,237-3,251, 2002.
- 764 Mu, M., Randerson, J. T., van der Werf, G. R., Giglio, L., Kasibhatla, P., Morton, D., Collatz, G.
765 J., DeFries, R. S., Hyer, E. J., Prins, E. M., Griffith, D. W. T., Wunch, D., Toon, G. C.,
766 Sherlock, V., and Wennberg, P. O.: Daily and 3-hourly variability in global fire emissions
767 and consequences for atmospheric model prediction of carbon monoxide, *J. Geophys. Res.*,
768 116, D24303, doi:10.1029/2011JD016245, 2011.
- 769 Neal, L. S., Dalvi, M., Folberth, G., McInnes, R. N., Agnew, P., O'Connor, F. M., Savage, N. H.,
770 and Tilbee, M.: A description and evaluation of an air quality model nested within global
771 and regional composition-climate models using MetUM, *Geosci. Model Dev.*, 10, 3941-3962,
772 doi:10.5194/gmd-10-3941-2017, 2017.
- 773 Peters-Lidard, C. D., Houser, P. R., Tian, Y., Kumar, S. V., Geiger, J., Olden, S., Lighty, L., Doty,
774 B., Dirmeyer, P., Adams, J., Mitchell, K., Wood, E. F., and Sheffield, J.: High-performance
775 Earth system modeling with NASA/GSFC's Land Information System, *Innovations in*
776 *Systems and Software Engineering*, 3, 157–165, 2007.
- 777 Peters-Lidard, C. D., Kemp, E. M., Matsui, T., Santanello, J. A., Kumar, S. V., Jacob, J. P., Clune,
778 T., Tao, W.-K., Chin, M., Hou, A., Case, J. L., Kim, D., Kim, K.-M., Lau, W., Liu, Y., Shi,
779 J., Starr, D., Tan, Q., Tao, Z., Zaitchik, B. F., Zavodsky, B., Zhang, S. Q., and Zupanski,
780 M.: Integrated modeling of aerosol, cloud, precipitation and land processes at satellite-
781 resolved scales. *Environmental Modeling & Software* 67, 149-159, 2015.
- 782 Rienecker, M. M., Suarez, M. J., Gelaro, R., Todling, R., Bacmeister, J., Liu, E., Bosilovich, M.
783 G., Schubert, S. D., Takacs, L., Kim, G.-K., Bloom, S., Chen, J., Collins, D., Conaty, A., da
784 Silva, A., Gu, W., Joiner, J., Koster, R. D., Lucchesi, R., Molod, A., Owens, T., Pawson, S.,
785 Pegion, P., Redder, C. R., Reichle, R., Robertson, F. R., Ruddick, A. G., Sienkiewicz, M.,
786 and Woollen, J.: MERRA - NASA's Modern-Era Retrospective Analysis for Research and
787 Applications, *J. Climate*, 24, 3624–3648, 2011.
- 788 Seo, J., Youn, D., Kim, J. Y., and Lee, H.: Extensive spatiotemporal analyses of surface ozone and
789 related meteorological variables in South Korea for the period 1999-2010, *Atmos. Chem.*
790 *Phys.*, 14, 6395-6415, doi:10.5194/acp-14-6395-2014, 2014.
- 791 Shi, J. J., Matsui, T., Tao, W.-K., Tan, Q., Peters-Lidard, C. D., Chin, M., Pickering, K., Guy, N.,
792 Lang, S., and Kemp, E. M.: Implementation of an aerosol-cloud microphysics-radiation
793 coupling into the NASA Unified WRF: Simulation results for the 6-7 August 2006 AMMA
794 Special Observing Period, *Q. J. R. Meteorol. Soc.*, doi:10.1002/qj.2286, 2014.
- 795 Stockwell, W. R., Middleton, P., Chang, J. S., and Tang, X.: The Second Generation Regional
796 Acid Deposition Model Chemical Mechanism for Regional Air Quality Modeling, *J.*
797 *Geophys. Res.*, 95, 16343-16367, 1990.
- 798 Tao, W.-K., Shi, J. J., Chen, S. S., Lang, S., Lin, P.-L., Hong, S.-Y., Peters-Lidard, C., and Hou,
799 A.: The impact of microphysical schemes on hurricane intensity and track, *Asia-Pacific J.*
800 *Atmos. Sci.*, 47, 1–16, 2011.
- 801 Tao, Z., Santanello, J. A., Chin, M., Zhou, S., Tan, Q., Kemp, E. M., and Peters-Lidard, C. D.:
802 Effect of land cover on atmospheric processes and air quality over the continental United
803 States – A NASA Unified WRF (NU-WRF) model study, *Atmos. Chem. Phys.*, 13, 6207-
804 6226, doi: 10.5194/acp-13-6207-2013, 2013.
- 805 Tao, Z., Yu, H., and Chin, M.: Impact of transpacific aerosol on air quality over the United States:
806 A perspective from aerosol-cloud-radiation interactions, *Atmos. Environ.*, 125, 48-60,
807 doi:10.1016/j.atmosenv.2015.10.083, 2016.



- 808 Tao, Z., Braun, S. A., Shi, J. J., Chin, M., Kim, D., Matsui, T., and Peters-Lidard, C. D.:
809 Microphysics and radiation effect of dust on Saharan air layer: An HS3 case study, *Mon. Wea.*
810 *Rev.*, 146, 1813-1835, doi:10.1175/MWR-D-17-0279.1, 2018.
- 811 Tie, X., Brasseur, G., and Ying, Z.: Impact of model resolution on chemical ozone formation in
812 Mexico City: application of the WRF-Chem model, *Atmos. Chem. Phys.*, 10, 8983-8995,
813 doi:10.5194/acp-10-8983-2010, 2010.
- 814 Valari, M. and Menuet, L.: Does an increase in air quality model's resolution bring surface ozone
815 concentrations closer to reality?, *J. Atmos. Oceanic Tech.*, 25, 1955-1968,
816 doi:10.1175/2008JTECHA1123.1, 2008.
- 817 van der Werf, G. R., Randerson, J. T., Giglio, L., Collatz, G. J., Mu, M., Kasibhatla, P. S.,
818 Morton, D. C., DeFries, R. S., Jin, Y., and van Leeuwen, T. T.: Global fire emissions and the
819 contribution of deforestation, savanna, forest, agricultural, and peat fires (1997–2009),
820 *Atmos. Chem. Phys.*, 10, 11707-11735, doi:10.5194/acp-10-11707-2010, 2010.
- 821 Wang, W.-N., Cheng, T.-H., Gu, X.-F., Chen, H., Guo, H., Wang, Y., Bao, F.-W., Shi, S.-Y., Xu,
822 B.-R., Zuo, X., Meng, C., and Zhang, X.-C.: Assessing spatial and temporal patterns of
823 observed ground-level ozone in China, *Sci. Rep.*, 7, 3651, doi:10.1038/s41598-017-03929-
824 w, 2017.
- 825 Yu, Man: An assessment of urbanization impact on China by using WRF-Chem and configuration
826 optimization, PhD (Doctor of Philosophy) thesis, University of Iowa,
827 <https://doi.org/10.17077/etd.lzfu2tj8>, 2014.
- 828 Zhao, X. J., Zhao, P. S., Xu, J., Meng, W., Pu, W. W., Dong, F., He, D., and Shi, Q. F.: Analysis
829 of a winter regional haze event and its formation mechanism in the North China Plain, *Atmos.*
830 *Chem. Phys.*, 13, 5685-5696, doi:10.5194/acp-13-5685-2013, 2013.
- 831 Zou, Y., Wang, Y., Zhang, Y., and Koo, J.-H.: Arctic sea ice, Eurasia snow, and extreme winter
832 haze in China, *Sci. Adv.*, 3, e1602751, 2017.
- 833
834
835
836
837



838 Table 1. Information of Air Quality Observation Sites

839

Site Name	Symbol	Longitude	Latitude	Altitude (m)	Setting
Baoding	BD	115.441	38.824	4	Urban
Beijing Tower	BJT	116.372	39.974	44	Urban
Chengde	CD	117.925	40.973	395	Urban
Caofeidian	CFD	118.442	39.270	11	Urban
Cangzhou	CZ	116.779	38.286	12	Urban
Datong	DT	113.389	40.089	1058	Urban
Gu An	GA	115.734	39.149	21	Rural
Hejian	HJ	116.079	38.423	66	Urban
Hengshui	HS	115.656	37.742	77	Urban
Langfang	LF	116.689	39.549	19	Urban
Lingshan	LS	115.431	39.968	116	Rural
Longtan Lake	LTH	116.430	39.870	31	Urban
Qian An	QA	118.800	40.100	54	Urban
Qinhuangdao	QHD	119.570	39.950	2.4	Urban
Shijiazhuang	SJZ	114.529	38.028	70	Urban
Shuangqing Road	SQL	116.338	40.007	58	Urban
Tanggu	TG	117.717	39.044	13	Urban
Tianjin	TJ	117.206	39.075	2	Urban
Tangshan	TS	118.156	39.624	14	Urban
Xianghe	XH	116.962	39.754	9	Suburban
Xinglong	XL	117.576	40.394	879	Rural
Yangfang	YF	116.126	40.147	78	Suburban
Yanjiao	YJ	116.824	39.961	26	Suburban
Zhangjiakou	ZJK	114.918	40.771	777	Urban
Zhuozhou	ZZ	115.988	39.460	48	Suburban

840

841

842

843 Table 2. Comparisons of occurrences of exceedances of China's National Ambient Air Quality
 844 Standards between observations and simulations*

845

	Frequency	Class 1	Class 2	Obs.	45-km	15-km	5-km
CO	Hourly	10	10	1,150	0	0	0
O ₃	Hourly	160	200	3,684	24,807	10,283	9,880
NO _x	Hourly	250	250	9,009	14	520	3,003
SO ₂	Hourly	150	500	393	0	2	39
PM _{2.5}	24-hours	35	75	1,343	1,720	1,610	1,574
PM ₁₀	24-hours	50	150	2,834	2,067	1,617	1,676

846

847

848

849

* Class 1/2 standards are for rural/suburban-urban, respectively. Units are $\mu\text{g m}^{-3}$.



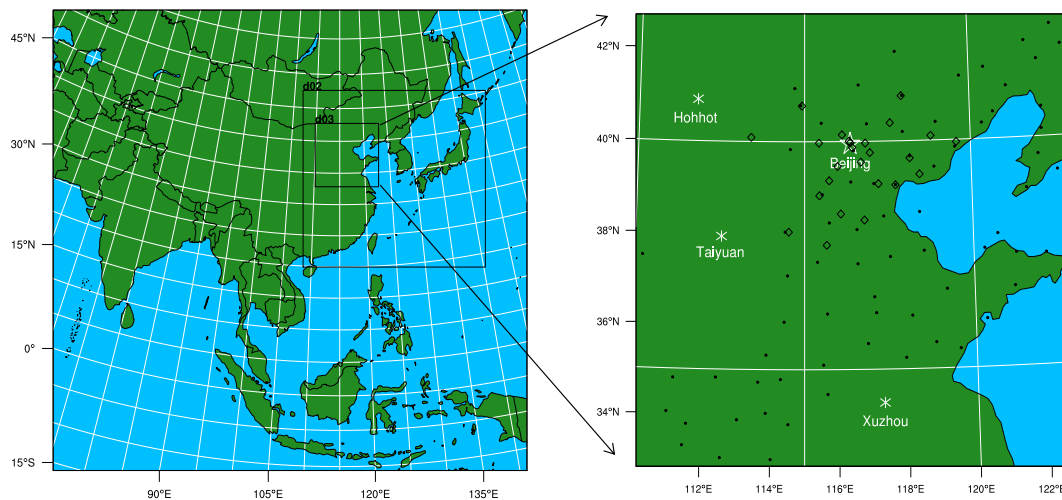
850 Table 3. Regional total emissions and average meteorology and air quality at various resolutions
 851

Variables	Period	45-km	15-km	5-km
Biogenic Isoprene (tons)	Annual	740,562	869,317	862,199
Dust (tons)	Annual	2,431	4,485	3,910
Sea salt (tons)	Annual	548	1,287	1,417
Surface air temperature (K)	January	268	267	268
	July	300	299	299
Surface wind speed (m s ⁻¹)	January	2.92	2.73	2.51
	July	1.70	1.54	1.52
SWDOWN (W m ⁻²)	January	124	117	117
	July	249	242	250
PBLH (m)	January	333	338	331
	July	627	595	574
CWP (g m ⁻²)	January	4.34	11.3	11.1
	July	41.4	56.8	55.2
Surface O ₃ (ppbv)	January	37.5	39.4	39.5
	July	86.8	68.8	69.2
Surface NO _x (ppbv)	January	19.8	14.9	15.0
	July	9.03	8.32	7.96
Surface CO (ppmv)	January	0.600	0.521	0.526
	July	0.444	0.336	0.308
Surface SO ₂ (ppbv)	January	16.6	12.9	13.2
	July	10.2	6.55	6.23
Surface PM _{2.5} (µg m ⁻³)	January	70.9	59.8	61.0
	July	89.3	58.0	46.2
Surface PM ₁₀ (µg m ⁻³)	January	102	88.1	89.6
	July	108	74.9	60.3

852
 853



854



855

856

857

858

859

860

861

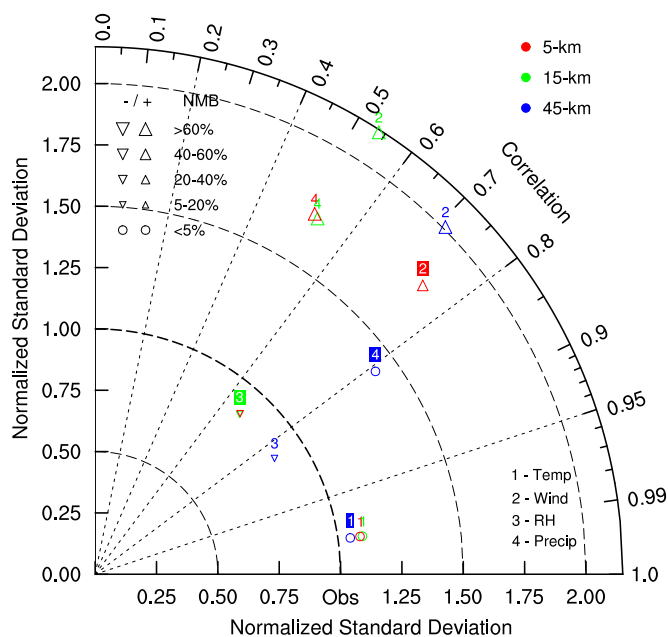
862

863

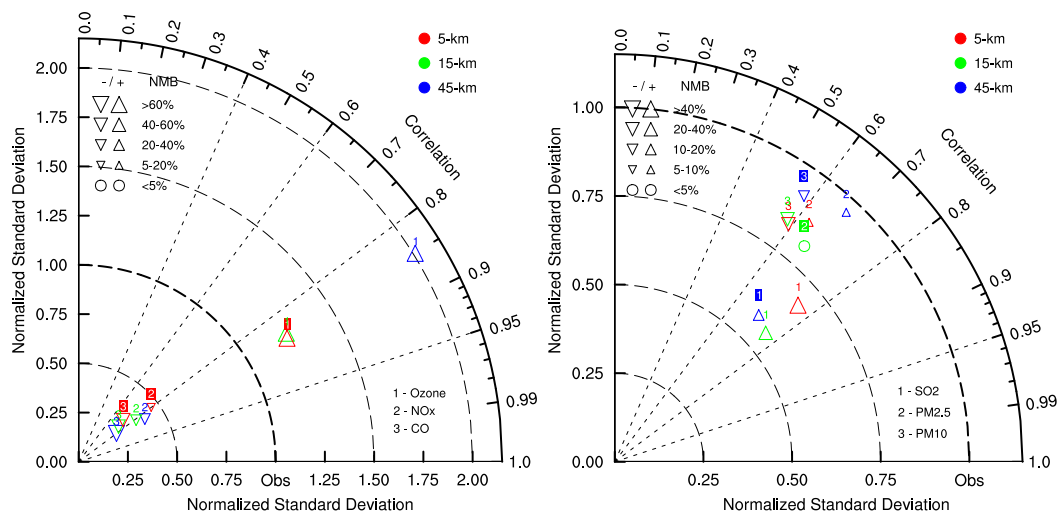
Figure 1. NU-WRF domain set-up. Left panel is the nested MICS-Asia domains; right panel is the enlarged NCP domain (d03) with diamonds representing the air quality monitoring sites and black dots denoting for the meteorological stations. Locations of four cities are marked for position reference.



864



865

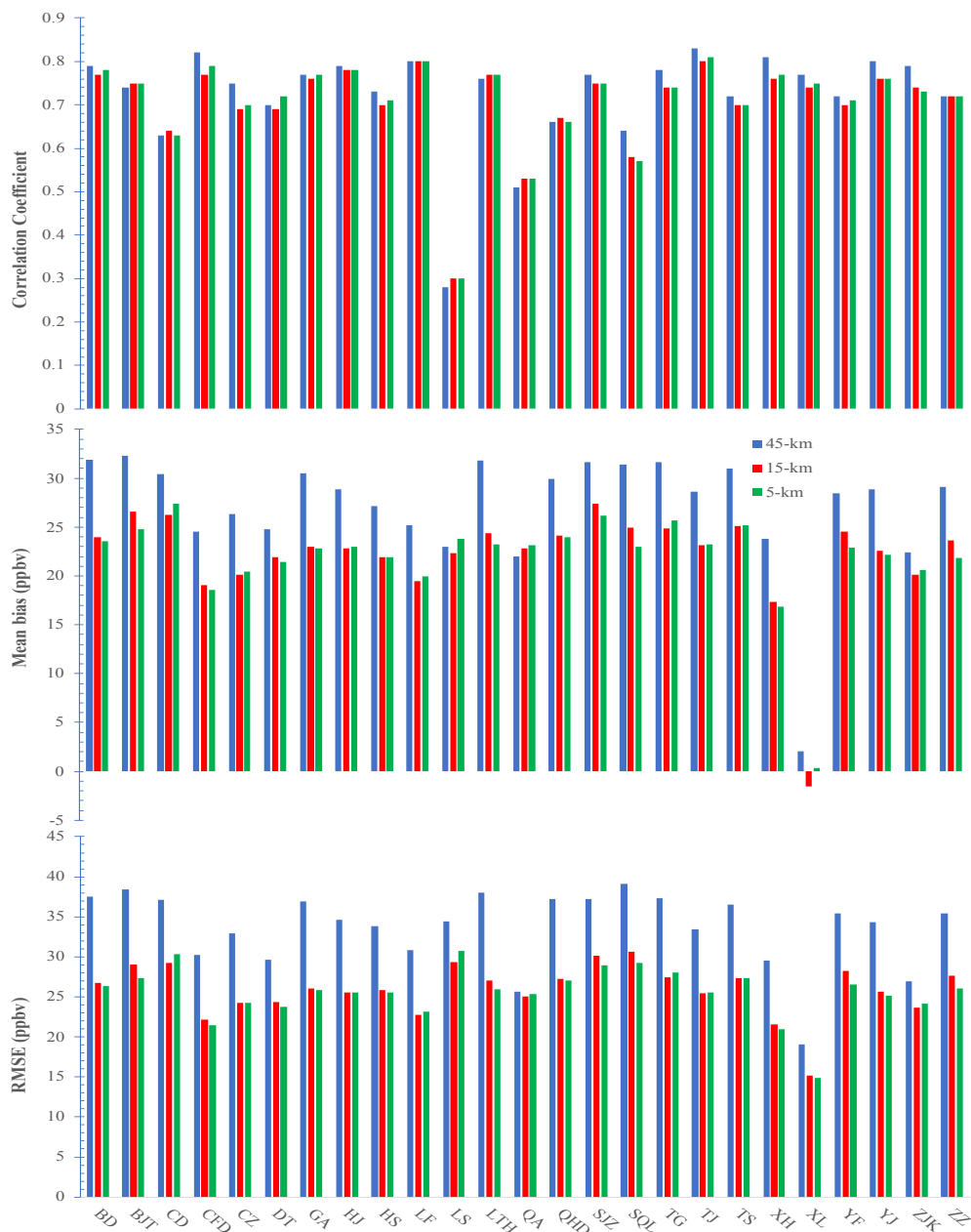


866
 867
 868
 869
 870
 871

Figure 2. Taylor diagram for evaluations of NU-WRF performances on meteorology (top row) and air quality (bottom row) simulations at three resolutions



872

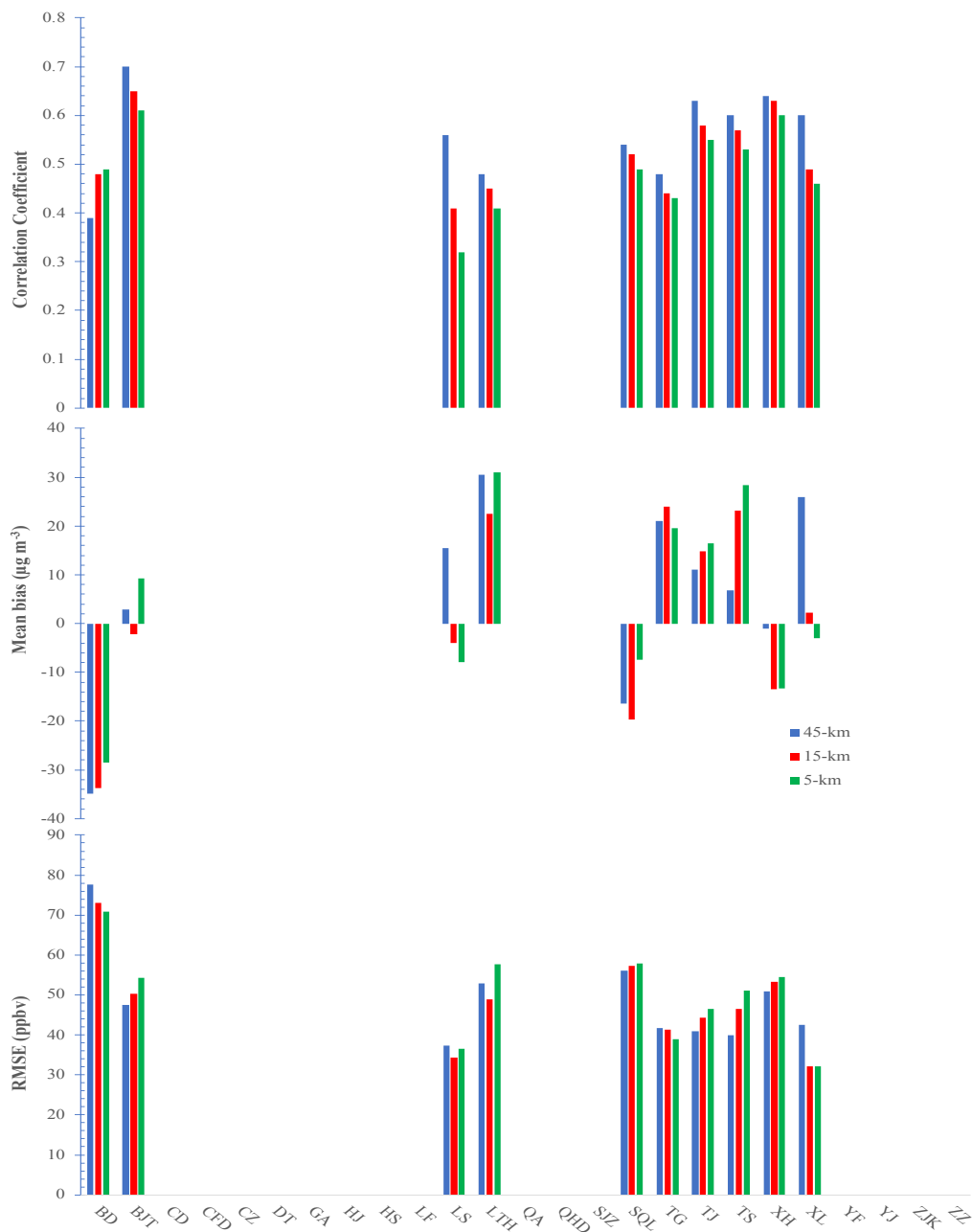


873
 874
 875
 876
 877

Figure 3. Comparisons of *MB*, *RMSE*, and correlation coefficient (*r*) of surface O₃ from different horizontal resolutions at each air quality monitoring site



878

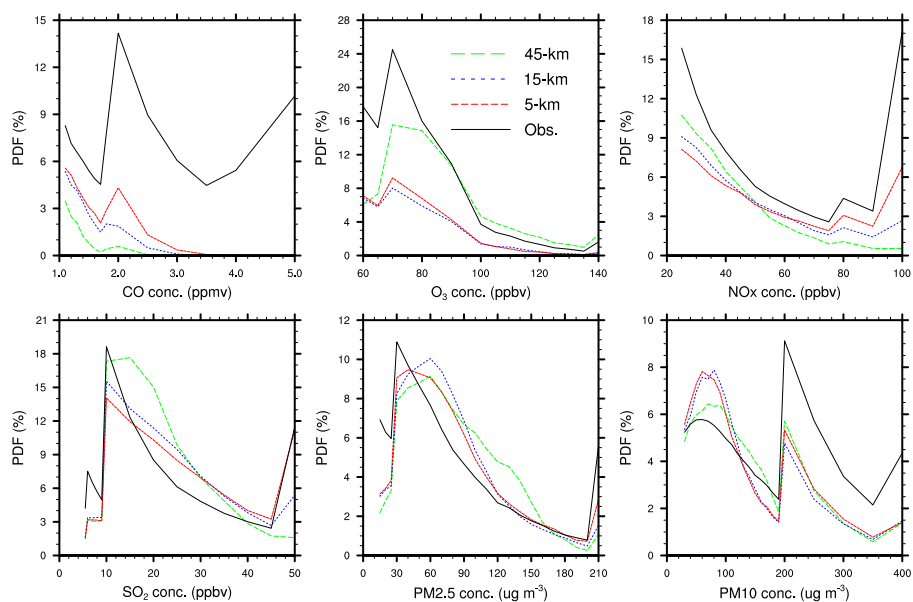


879
 880
 881
 882
 883

Figure 4. Comparisons of *MB*, *RMSE*, and correlation coefficient (*r*) of surface PM_{2.5} from different horizontal resolutions at each air quality monitoring site (blank space indicates no data are available)

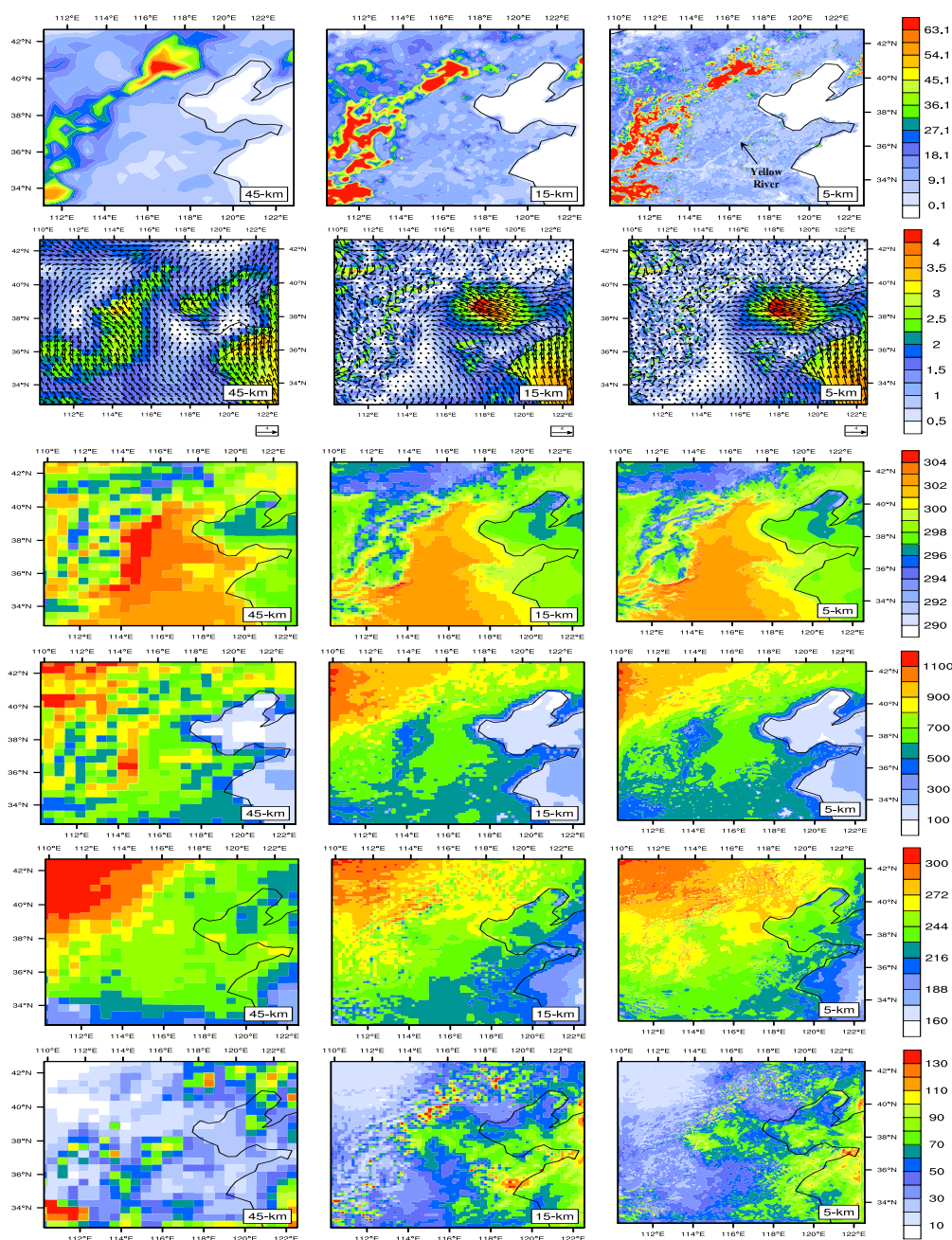


884

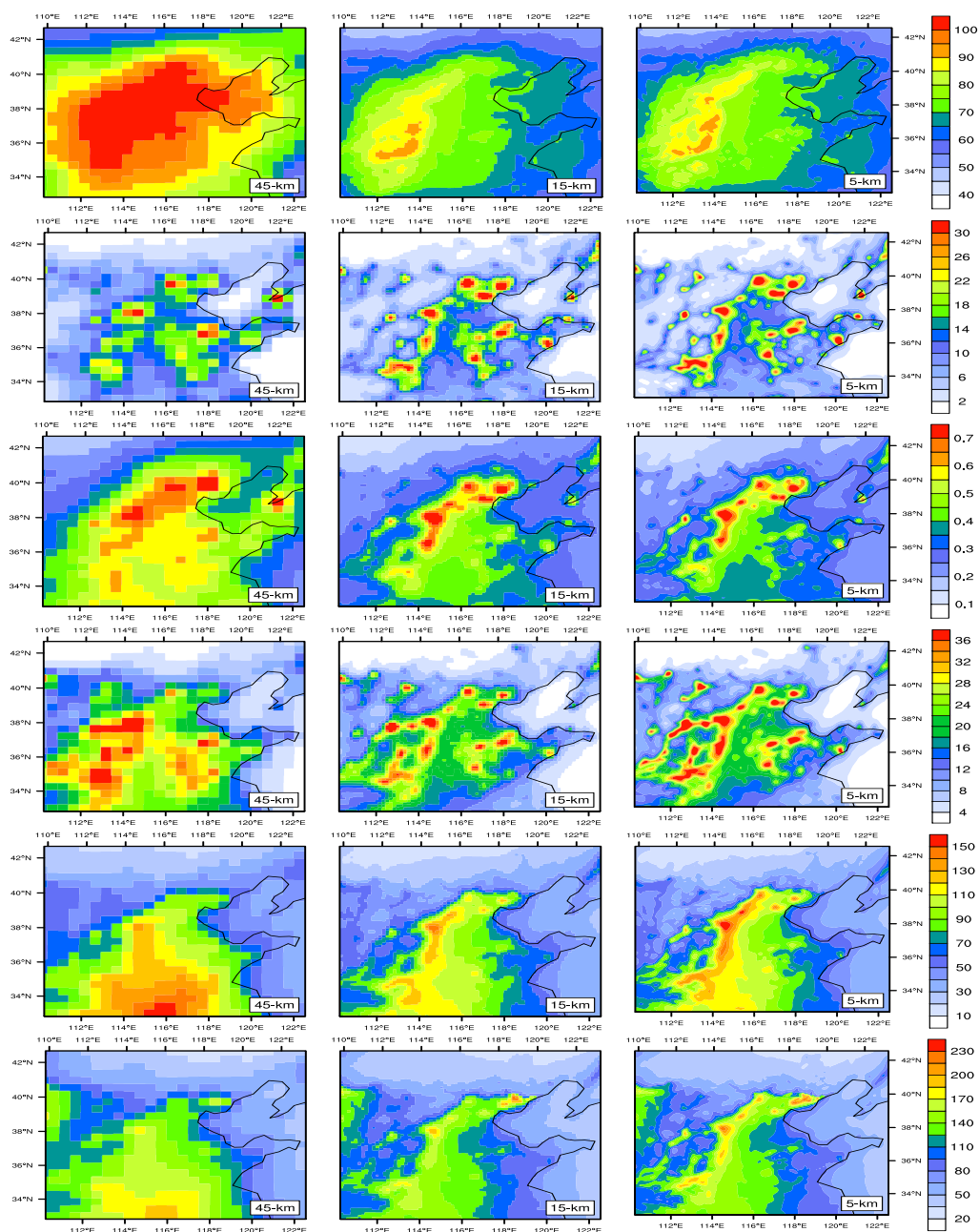


885
886
887
888

Figure 5. Probability density function (PDF) plots for hourly concentrations of surface air quality

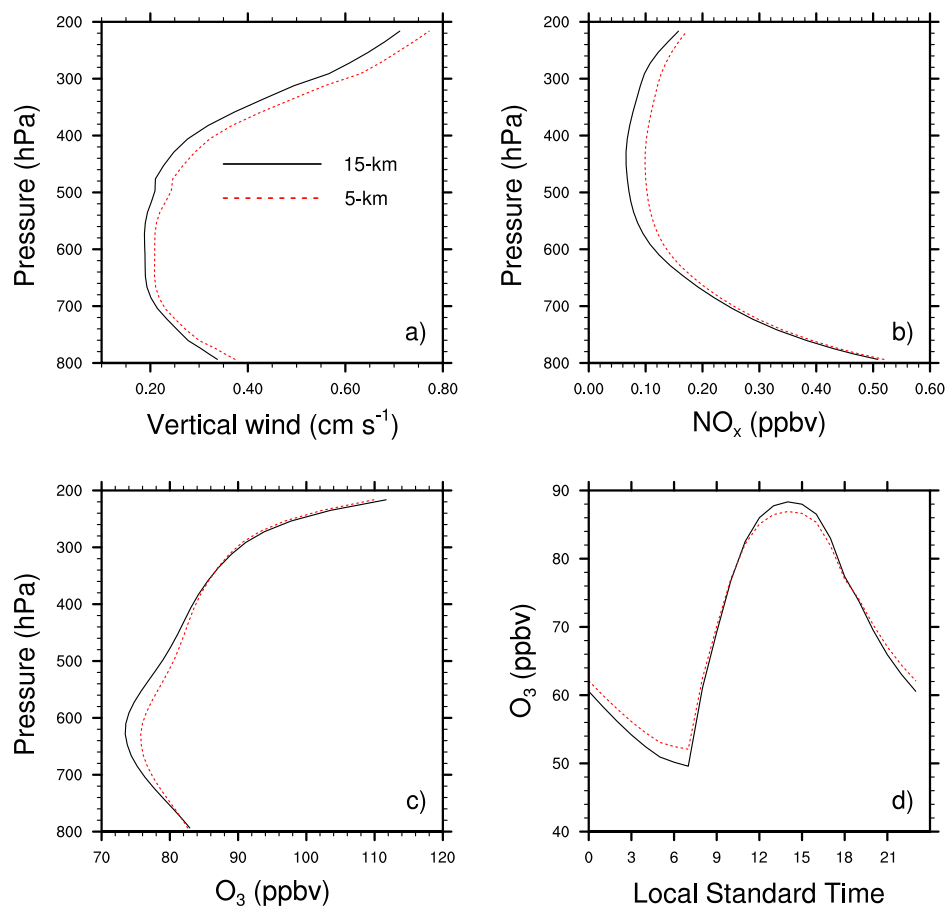


889
890 Figure 6. Simulated emissions and July average meteorology from 3 grids: 1st row = isoprene
891 emissions ($\text{mol km}^{-2} \text{hr}^{-1}$) from biogenic sources on a typical summer day; 2nd row = surface wind
892 vector with the shade representing wind speed (m s^{-1}); 3rd row = surface air temperature (K); 4th
893 row = PBLH (m); 5th row = SWDOWN (W m^{-2}); 6th row = CWP (g m^{-2}).
894



895
896
897
898
899
900

Figure 7. Simulated January (SO_2 , $\text{PM}_{2.5}$, and PM_{10}) and July (O_3 , NO_x , and CO) surface average air quality from 3 grids: 1st row = O_3 (ppbv); 2nd row = NO_x (ppbv) 3rd row = CO (ppmv); 4th row = SO_2 (ppbv); 5th row = $\text{PM}_{2.5}$ ($\mu\text{g m}^{-3}$); 6th row = PM_{10} ($\mu\text{g m}^{-3}$).



901
902
903
904

Figure 8. Domain average profiles of vertical wind, NO_x, and O₃ concentrations (Panels a–c) and domain average diurnal variations of surface O₃ over July.